UNIVERSITÀ DEGLI STUDI DI PADOVA

Dipartimento di Fisica e Astronomia "Galileo Galilei"

Corso di Laurea in Astronomia

Tesi di Laurea Triennale

Comparative Analysis of TeV Blazars Emissive Characteristics

Relatore

Prof. Michele Doro

Correlatrice

Prof.ssa Elisa Prandini

Laureanda

Martina Morrone

Anno Accademico 2023/2024

Abstract

Blazars are Active Galactic Nuclei (AGN) characterized by jets of relativistic particles that form a small angle with the line of sight. These highly energetic sources emit radiation through non-thermal processes across the entire electromagnetic spectrum. The analysis of their emissive properties is influenced by the observational band. The aim of this thesis is to analyze the emissive characteristics of blazars observed in the TeV band by IACTs (MAGIC, VERITAS, and H.E.S.S.) and to compare this population, comprising almost one hundred sources, with the blazar population observed in the GeV band by the *Fermi*-LAT space telescope, which includes thousands of members. The final goal was to extrapolate insights for future CTAO observations from the comparison between the two populations.

I blazar sono AGN (Active Galactic Nuclei) dotati di un getto di particelle relativistiche che forma un piccolo angolo con la linea di vista. Sono sorgenti molto energetiche che emettono radiazione secondo processi non termici in tutto lo spettro elettromagnetico. L'analisi delle caratteristiche emissive è condizionata dalla banda in cui si osserva. L'obiettivo di questa tesi è quello di analizzare le caratteristiche emissive dei blazar osservati nella banda TeV dai telescopi IACTs (MAGIC, VERITAS e H.E.S.S.) e confrontare questa popolazione, costituita da poco meno di un centinaio di sorgenti, con quella dei blazar osservati nella banda GeV dal telescopio spaziale *Fermi*-LAT, costituita invece da migliaia di sorgenti. Lo scopo finale è stato quello di estrapolare informazioni sulle future osservazioni di CTAO dal confronto delle due popolazioni.

Contents

Chapter 1

Introduction

Blazars are a class of Active Galactic Nuclei (AGNs) characterized by jets of relativistic particles aligned at a small angle with respect to the line of sight of the observer. These highly energetic sources emit non-thermal radiation across the entire electromagnetic spectrum, from radio waves to gamma rays. The analysis of their emission characteristics strongly depends on the wavelength band in which they are observed. Currently, observations in the GeV band, carried out by the Fermi-LAT space telescope, have cataloged thousands of blazars, while only 86 have been detected in the TeV band by ground-based Imaging Atmospheric Cherenkov Telescopes (IACTs). This discrepancy results in a fragmented understanding of blazars high-energy behavior, limiting the fully understanding of the physical mechanisms that drive their emissions. This thesis compares the two blazar populations observed in the GeV and TeV bands to identify and characterize their differences. The aim is to understand how these differences are influenced by both the energy ranges of the instruments and the intrinsic emission properties of the blazars.

The upcoming Cherenkov Telescope Array Observatory (CTAO) is expected to significantly enhance sensitivity in the TeV range. Studying the universe at high energies involves a broad range of scientific topics, such as particle acceleration in relativistic jets, interactions between gamma rays and the Extragalactic Background Light (EBL), and the search for indirect signals of dark matter. Given this diversity of interests, planning future observations of CTAO requires careful consideration of how to maximize the scientific output in relation to the specific goals being pursued. Up to now, IACTs have primarily adopted a strategy focused on the observation of individual sources, and, in the case of blazars, often prioritizing observations of blazar flares when triggered by alerts from other instruments operating in different energy bands. Due to this approach of focusing on specific sources already observed in other bands, the TeV sky remains largely unmapped because of the extensive observation time required for such a task. IACTs, being ground-based, are subject to atmospheric limitations, such as weather conditions, moonlight, and limited nighttime operation windows. Moreover, current generation of IACTs is characterized by a limited field of view. By contrast, Fermi-LAT, which operates continuously in space, has conducted full-sky surveys, mapping the entire sky in the GeV band. Aside from the galactic plane mapped by H.E.S.S. in a dedicated campaign, most of the extragalactic sky in the TeV range remains unexplored. Therefore, one of the main goals of CTAO is to conduct extragalactic surveys to map the TeV sky. This is a highly time-consuming task that requires scrupulous planning to identify the best observation strategy. Decisions must be made about which areas of the sky to prioritize, how extensive the survey should be, and how long each region should be

observed to maximize the scientific return. The need for accurate predictions requires *extrapolations* of as much information as possible in the TeV band, based on the observations already performed. These predictions allow for a more efficient use of observation time, enabling CTAO to balance targeted observations with broader sky surveys, thereby maximizing both the scientific and economic value of its campaigns.

Different methods can be applied to extrapolate the behavior of sources at TeV energies. Some approaches rely on extrapolating from *Fermi*-LAT data by assuming a power-law spectrum, while others use full SED modeling to predict TeV behavior. This thesis presents a different approach by offering a synoptic comparison of the GeV and TeV populations, which aids in making informed predictions about future observational strategies of CTAO. The ultimate goal is to provide estimates of how many GeV-detected blazars could potentially be observed in the TeV band by CTAO.

Summary

Chapter 2 introduces the theoretical background on blazars, detailing their properties, the physical processes driving their emissions. It also discusses the observational challenges related to detecting blazars in the gamma-ray band, along with an overview of gamma-ray instrumentation. The final section focuses on the tools and data platforms used to organize, analyze, and interpret the vast amount of data collected from blazar observations.

Chapter 3 describes the methodology used in the thesis. It outlines the procedure for selecting the blazars that compose the GeV and TeV samples and explains how the parameters used for comparison, such as synchrotron peak frequency, flux, and redshift, were selected and extracted.

Chapter 4 presents the comparison between the GeV and TeV blazar populations conducted in this thesis, comparing the distributions of synchrotron peak frequency, redshift, and synchrotron peak flux. The chapter ends with a prediction on future observations by CTAO.

Chapter 2

Blazar

Blazars are a type of **Active Galactic Nuclei** (AGNs). AGNs are structures located at the center of many galaxies, formed around a supermassive black hole (SMBH). Due to its strong gravitational field, a large portion of surrounding matter is attracted by the SMBH and forms a rotating accretion disk. Material falling into the disk heats up as it spirals toward the black hole and emits radiation, especially in the ultraviolet (UV) and X-ray wavelength. This radiation can excite nearby clouds of gas and dust, leading to the production of emission lines. These clouds are grouped into two distinct regions: the Broad Line Region (BLR) and the Narrow Line Region (NLR). The BLR is closer to the black hole, at around 0.01 to 1 light year, and consists of dense and fast moving clouds of gas emitting broad emission lines in the optical and UV. Further from the black hole, at distances of several hundreds light years, lies the NLR, where the gas clouds are less dense and move slower. As a result, the emission lines from the NLR are narrower. The central structure of the AGN is surrounded by a corona of ionized gas that produces X-rays. Beyond the corona, at a distance of a few parsecs from the SMBH, lies a dusty torus, a dense region of gas and dust that heats up due to the emission from the inner region and re-emits this energy in the infrared. A schematic representation of the AGN's structure is shown in figure 2.1.

About 10% of AGNs, besides accreting material, eject two jets of particles in opposite directions perpendicular to the rotation plane of the central black hole. These jets are powered by the intense magnetic fields near the SMBH and can accelerate particles to relativistic speeds, producing non-thermal radiation. When these jets are aligned towards Earth, relativistic beaming significantly amplifies their apparent brightness, making them some of the most luminous sources in the universe. The emission from the jets spans the entire electromagnetic spectrum, from radio waves to gamma rays, and is characterized by a strong, continuous component resulting from non-thermal emission processes. The formation of these jets is still under investigation, along with the processes responsible for particle acceleration.

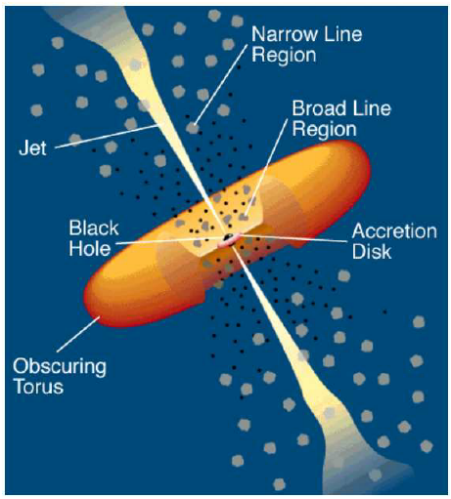

Figure 2.1: Illustration of the morphology of a jetted AGN. From Urry and Padovani 1995.

The emission mechanisms in the jet are also debated, with some models proposing leptonic processes, primarily involving electrons and positrons, while others suggest a hadronic origin, dominated by protons (Sol and Zech 2022). However, the relativistic particles accelerated within the jet are certainly responsible for the non-thermal emission.

The emissive characteristics of AGNs change depending on the angle at which the object is observed. For this reason, in the past, different types of AGNs were discovered and believed to belong to separate classes of emitters. The Unification Model of AGNs, first proposed by Urry and Padovani 1995, grouped these different classes together and explains the observed differences as a result of the orientation of the AGN, as illustrated in figure 2.2.
A primary distinction can be made based on the angle of the jets relative to the observer: blazars, whose jets are directed towards Earth, and other sources, referred to as radio galaxies, where the jets are oriented in a different direction.

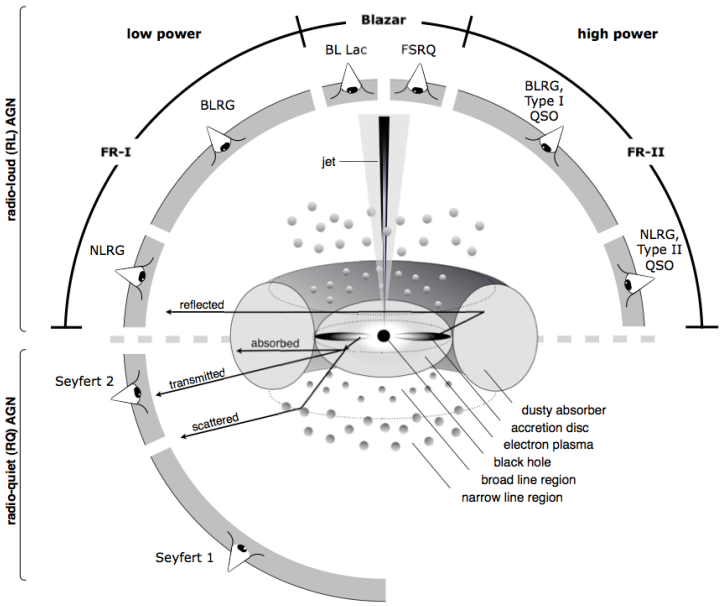

Figure 2.2: Scheme of the unification model of AGN proposed by Urry and Padovani 1995: the classification of the source depend on the orientation.

2.1 Blazars' Properties

Blazars are jetted AGNs with their jets forming a small angle with the line of sight. They are among the most energetic sources in the universe and emit across the entire electromagnetic spectrum, as shown in Figure 2.3, which plots the Spectral Energy Distribution (SED) for five different blazars. For all of them, the emission ranges from radio waves to gamma rays. They can be divided into two classes based on their observational characteristics:

- Flat Spectrum Radio Quasars (FSRQs), characterized by the presence of strong emission lines. This suggests that they are characterized by environments rich in gas and dust that contributes to the presence of a massive BLR.

- BL Lacertae objects (BL Lacs), which exhibit weak or absent emission lines. This suggests that they are in environments poor of gas and dust, explaining the absence or weakness of the BLR.

Not all blazars fit neatly into these two categories: some transitional objects exhibit properties of both BL Lacs and FSRQs (G. Ghisellini, Tavecchio, et al. 2011).

Regardless of the classification, the emission resulting from processes occurring in the jet is so intense that it almost completely obscures emissions from the other components of the blazar, such as the thermal emission from the accretion disk or the emission lines from surrounding gas clouds. In the case of BL Lacs, which have weak emission lines, this is particularly evident, and the emission is dominated by the continuous component across the entire spectrum. The Spectral Energy Distribution (SED) always has a double-peaked shape. The first peak can occur between 10^{12} Hz and 10^{17} Hz, and is attributed to synchrotron radiation emitted by relativistic electrons spiraling in the magnetic field of the jet. The origin of the second peak, located around $10^{21} - 10^{25}$ Hz, is less certain. It can be explained by inverse Compton scattering, where photons are boosted to higher energies by scattering with relativistic electrons responsible for the synchrotron emission. These emission mechanisms will be explained in more detail in 2.1.2.
BL Lacs blazars can be further divided into subcategories based on the position of the synchrotron peak. The classification is not univocal, and the following has been adopted in this thesis:

- Low-peaked BL Lac (LBL), if $\nu_{synch} \leq 10^{13.5}$ Hz (infrared)
- Intermediate-peaked BL Lac (IBL), if $10^{13.5} < \nu_{synch} \leq 10^{15}$ Hz (optic and UV)
- High-peaked BL Lac (HBL), if $\nu_{synch} > 10^{15}$ Hz (UV and X-ray)

Blazar Sequence

The relative intensity and position of the two peaks in the SED differ between FSRQs and BL Lacs, as does the overall luminosity. The Blazar Sequence, shown in Figure 2.3, is the phenomenological model used to describe how the SEDs of blazars evolve with luminosity, proposed in Fossati et al. 1998 for the first time. FSRQs are more luminous than BL Lacs, with a synchrotron peak at lower frequencies and a stronger inverse Compton peak, sometimes even orders of magnitude higher than the synchrotron peak. This large difference in peak intensities is quantified by the Compton dominance, which is the ratio of the IC peak flux to the synchrotron peak flux. BL Lacs are less luminous, dominated by synchrotron radiation, with the synchrotron peak occurring at higher frequencies and the IC peak is typically of similar intensity to the synchrotron peak, meaning they exhibit a Compton dominance close to unity.
When comparing the SEDs of different classes, a strong relationship can be observed between the position of the synchrotron peak and the position of the Inverse Compton (IC) peak in the characteristic double-peaked shape of the blazar SED. As the synchrotron peak shifts to higher energies, the IC peak also shifts to correspondingly higher frequencies. Therefore, the position of the synchrotron peak serves as a proxy for the entire SED, and the classification introduced earlier not only represents an observational distinction but also reflects the physical properties of the blazars.

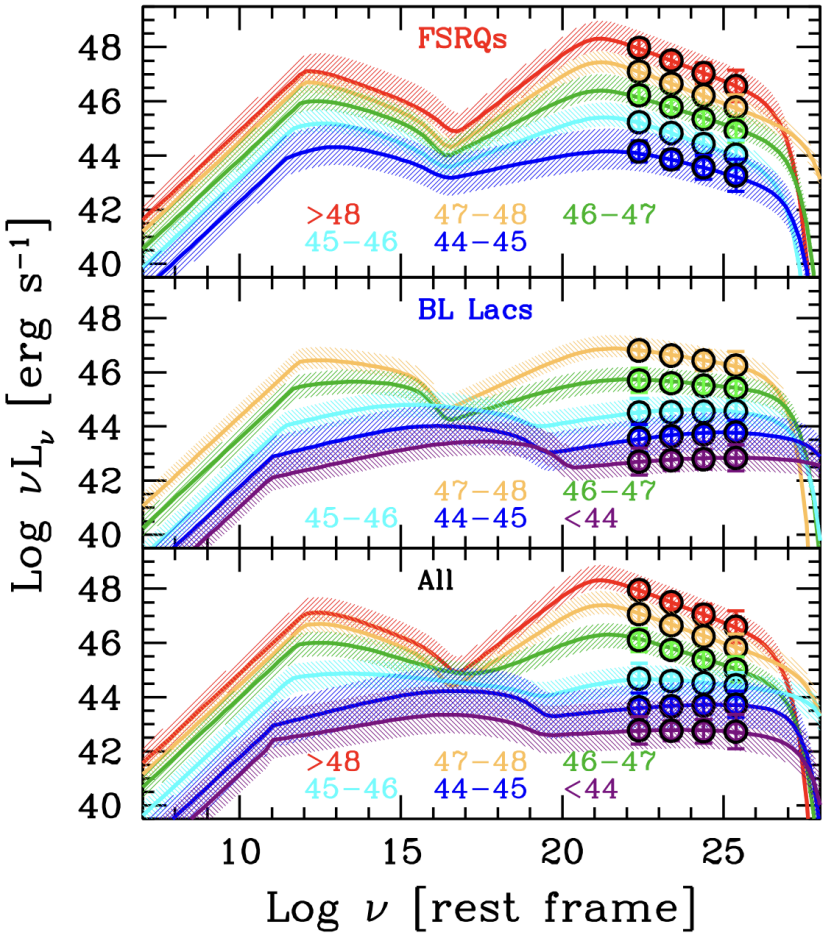

Figure 2.3: Blazar sequence, from G. Ghisellini, Righi, et al. 2017. The plot shows SED modeling for different blazars. The panel from top to bottom shows: first panel FSRQs; second panel BL Lacs; last panel the blazar sequence with BL Lacs and FSRQs.

2.1.1 Relativistic beaming and blazars variability

Blazars are among the most luminous sources in the universe. Their emission is amplified by relativistic beaming, a phenomenon that occurs when an emitting source is moving at relativistic speeds towards the observer. The relativistic beaming is a combination of the relativistic Doppler effect and the relativistic aberration of light.

The relativistic Doppler effect causes the shift in the frequency emitted by the source, ν_{emit}, according to the relation $\nu_{obs} = \delta \nu_{emit}$, where δ is the Doppler factor, given by:

$$\delta = \frac{1}{\Gamma(1 - \beta \cos\theta)}$$

In this expression, $\Gamma = (1-\beta^2)^{-1/2}$ is the Lorentz factor, $\beta = v/c$, the velocity of the emitting particles as a fraction of the speed of light, and θ is the angle between the direction of motion of the source and the line of sight of the observer. Since the source is approaching (the jet pointed towards Earth), the emitted frequency is shifted to higher energy values.

Relativistic aberration is the transformation of the emission angle of the light. The angle θ, at which photons are emitted relative to the line of sight, is reduced when the source is approaching. In the ultra-relativistic limit, this angle tends towards zero. As a result, the emission from the jet is highly

collimated along the line of sight, and the energy of the emitted radiation is significantly increased. The combination of these effects leads to an amplification of the observed luminosity of blazars. The observed luminosity is related to the emitted luminosity by the following relation:

$$L_{\text{observed}} \propto \delta^4 L_{\text{emitted}}$$

where the factor δ^4 accounts for the amplification due to both the frequency shift and the collimation of the emission due to the relativistic effect.

Blazars variability

Many blazars exhibit variable emission across different wavelengths. The variability can occur on timescales ranging from minutes to years:

- Long-term variability (months to years), like the case of the PG 1553+113, which exhibits periodic gamma-ray variability with a cycle of approximately 2.2 years (H. Abe et al. 2024).
- Short-term variability (days to weeks), like the case of BL Lacertae, the prototype of the BL Lac class, that shows variability on timescales of days and weeks across all spectral bands (Hinrichs, Acharyya, and Sadun 2023).
- Intra-night variability (minutes to hours), like the case of Markarian 421, which is known for its rapid flux changes within a single night. It exhibits some of the fastest variability among blazars, with flux variations occurring on timescales of minutes to a few hours, especially in the X-ray and gamma-ray bands (S. Abe et al. 2023).

Flares of blazars are variability events where a rapid increase in radiation flux is observed, followed by an equally quick decay. The origin of flares is still uncertain, with several mechanisms proposed to explain them. One possibility is that shock waves traveling through the jet accelerate particles, leading to an increase in radiation. Another one suggests that magnetic reconnection within the jet releases large amounts of energy in short periods, producing flares. Additionally, the injection of new particles into the jet may cause a sudden increase in radiation. These processes lead to changes in the emitted radiation, which are then significantly amplified by relativistic beaming. The study of these transient events provides information about the dynamic evolution of jets in blazars.

2.1.2 Non-thermal Emission Mechanisms

The continuous non-thermal radiation observed in blazars is primarily produced by particles accelerated to relativistic speeds within the jet. The models proposed to explain the emission are:

- **Hadronic model**: In this scenario, the high-energy emission is generated by relativistic hadrons, primarily protons, within the jet. These protons interact either with external photons (such as those from the accretion disk or BLR) or with synchrotron photons produced within the jet. These interactions can lead to processes such as proton-proton collisions and photo-meson production. This model requires strong magnetic fields to accelerate the particles, as hadrons

are heavier than leptons. However, it struggles to explain the observed rapid variability of blazars, as the timescales for hadronic interactions are typically too long.

- **Leptonic model**: The primary drivers of high-energy emission are relativistic electrons and positrons. These particles generate low-energy synchrotron radiation by spiraling in the magnetic fields of the jet. The same relativistic particles then scatter these synchrotron photons, or photons from an external radiation field, to higher energies through inverse Compton scattering. Leptonic models effectively explain the rapid variability observed in blazars, as the IC scattering process can occur on very short timescales However, these models often struggle to account for the most extreme frequencies in the very high-energy gamma-ray range, where hadronic processes may need to be used.

In this thesis, the leptonic model is considered the primary mechanism for explaining the non-thermal emission in blazars, where the first peak originates from the synchrotron radiation and the second peak from the inverse compton (IC) processes. A scheme of a leptonic model explaining the double-peak shape of SED blazar is shown in 2.4

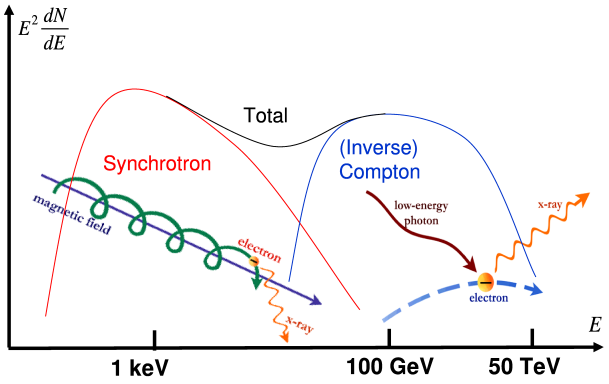

Figure 2.4: SSC scheme model, from De Angelis, Mansutti, and Persic 2008.

Synchrotron radiation

According to classical electrodynamics, when a particle with charge q and mass m accelerates or decelerates, it emits energy in the form of electromagnetic radiation. The total power P radiated by a non-relativistic particle is given by the *Larmor formula*:

$$P = \frac{2}{3}\frac{q^2 a^2}{c^3}$$

For relativistic particles, synchrotron radiation arises from the acceleration of charged particles moving at relativistic speeds in the presence of a magnetic field. Under the influence of the Lorentz force, the motion becomes helical, with a gyration frequency:

$$\omega_B = \frac{eB}{\gamma mc}$$

The radiated power for a relativistic particle can be described by the relativistic version of the Larmor formula:

$$P_{\text{synch}} = \frac{2}{3}\frac{e^4 B^2 \gamma^2 v_\perp^2}{m^2 c^5}$$

This shows that the power radiated increases with the square of the Lorentz factor γ. By expressing the magnetic field B in terms of the energy density U_B, and using the Thomson scattering cross-section σ_T, we arrive at the final expression for the synchrotron power:

$$P_{\text{synch}} = \frac{4}{3}\sigma_T c U_B \gamma^2$$

This formula indicates that the radiated power grows significantly with increasing γ, making synchrotron radiation a dominant process in high-energy astrophysical environments like blazars.

Inverse Compton

The Inverse Compton is a scattering process electron-photon (or positron-photon), in which the photon gains energy from the electron according to the conservation of momentum.

$$e_0^\pm + \gamma_0 \rightarrow e^\pm + \gamma \tag{2.1}$$

The cross section of the process can be described in two regimes, depending on whether the energy of the target photon is negligible compared to the electron rest energy $m_e c^2$ (Thomson regime) or not negligible (Klein-Nishina regime).
Since the variation in the photon energy in the rest frame and in the comoving one is negligible, the power gained by the photon (equal to the energy loss rate of the electron) is:

$$P_{Compton} = \frac{dE_{rad}}{dt} = \frac{4}{3} c \sigma_T \beta^2 \gamma^2 U_{ph} \tag{2.2}$$

Synchrotron Self Compton

The Synchrotron Self-Compton (SSC) model is the simplest model to describe the high energy peak in the blazar SED. In this model, the same population of relativistic electrons within the jet is responsible for both generating low-energy synchrotron radiation and upscattering those photons to higher energies through the inverse Compton process. The relativistic electrons produce synchrotron radiation, which forms the first peak. These synchrotron photons, initially emitted at low energies (radio to optical or X-ray bands), serve as the target photon field for inverse Compton scattering by the electrons that produced them. The scattered photons are boosted to higher frequency. This model well explain the SED shape of BL Lacs, where external photon fields produced in the region around the SMBH are negligible.

External Compton

The External Compton (EC) model assumes that relativistic electrons in the jet interact with external photon fields. These external photons are produced by several regions around the jet, such as the accretion disk, the broad-line region (BLR), or the dusty torus. The energy of these external photons can

vary; for example, photons from the accretion disk, often referred to as the blue bump, are typically in the ultraviolet or optical range, while photons from the BLR or dusty torus can be in the infrared. As a result, the EC process depends on the energy of the external photon field and the interaction conditions, which can significantly influence the energy of the emitted radiation. This model fits well with FSRQs, where emission from regions outside the jet, such as the accretion disk or BLR, creates an intense radiation field, providing enough seed photons for the EC process.

2.2 Blazar observation

Unlike controlled laboratory environments, where conditions can be adjusted and experiments replicated, the cosmos offers only one opportunity to observe each event and a single point of view to study any given object. This limitation makes it useful to collect multi-wavelength data, in order to capture as much information as possible across different parts of the electromagnetic spectrum. Such an approach is extremely important in the observation of blazars because their emission spans the entire electromagnetic spectrum, and each energy band provides unique insights into their physical properties and emission processes. By integrating data from multiple wavelengths, the mechanisms driving blazar emissions, such as particle acceleration in jets and interactions with surrounding material, can be better understood. The detection techniques differ across energy bands, each with its own specific limitations and advantages. Creating a comprehensive multi-wavelength view of a blazar involves collecting and analyzing photometric data, which are subject to various biases depending on the instruments used and the observation conditions. Moreover, the variability across different energy bands, particularly in high-energy emissions, adds another layer of complexity, requiring nearly simultaneous observations to accurately model the physical conditions within the jet.

In this thesis, the focus is on analyzing blazar emission in the gamma-ray band. While radio, optical, infrared, and X-ray observations have well-established strategies that have been refined over the years, gamma-ray astronomy is more recent and presents significant challenges, which will be explained in the following sections.

Gamma-ray astronomy

The gamma radiation comes from non-thermal emission processes by galactic and extragalactic objects. It is the highest energy portion of the electromagnetic spectrum, going from 100 keV to PeV. Due to this wide range, it is useful to define sub-bands according to energy intervals, as the following:

- High Energy (HE) 0.5 MeV - 100 GeV
- Very High Energy (VHE) 100 GeV - 30 TeV
- Ultra High Energy (UHE) 30 TeV - 30 PeV
- Extreme High Energy (EHE) >30 PeV

These intervals are strongly related to the detection technique and effect, as we will see in the next paragraph.

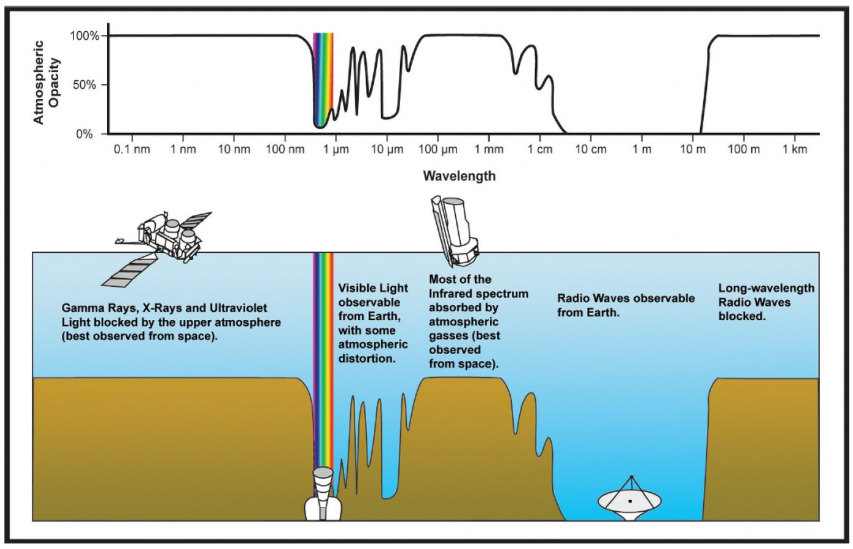

Figure 2.5: Atmospheric opacity for the electromagnetic spectrum, alongside the principal observational techniques. Image Credits: NASA.

EBL absorption

While propagating through space, gamma photons interact with cosmic backgrounds, either being scattered and therefore losing energy, or getting absorbed, reducing the observed flux. The most significant effect is due to the interaction with **Extragalactic Background Light** (*EBL*) (Cooray 2016), which consists of all accumulated radiation from star formation, galaxy evolution, and other cosmic sources since the Big Bang, extending across wavelengths from UV to infrared (IR). It is the second most intense background after the *Cosmic Microwave Background* (CMB), as shown in figure 2.6.

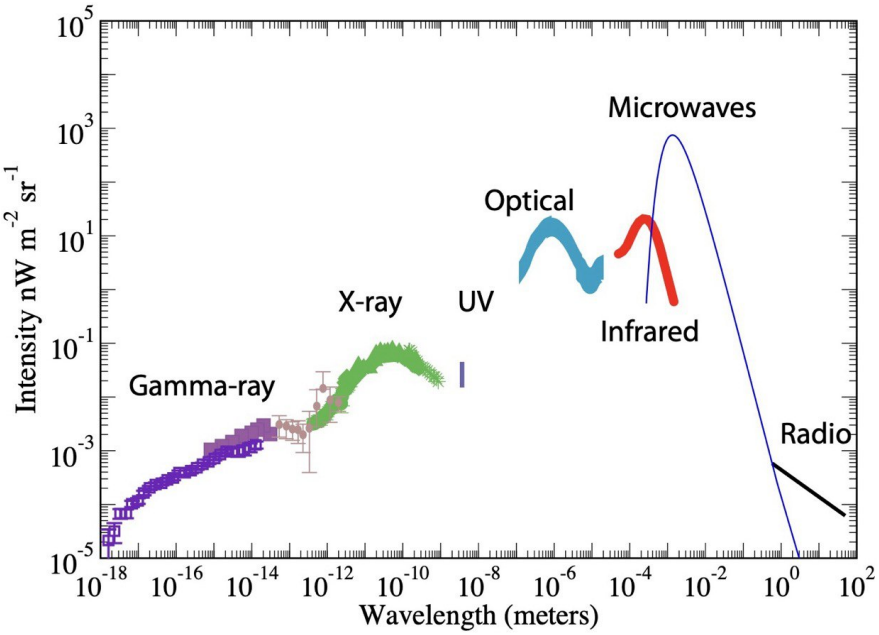

Figure 2.6: Intensity of Cosmic Background. From (Cooray 2016).

When a gamma photon γ interacts with an EBL photon γ', it leads to electron-positron pair production: $\gamma+\gamma' \rightarrow e^+ + e^-$. The cross-section for pair production is a function of the gamma photon energy

E_γ. The threshold at which absorption becomes significant is around ~ 100 GeV (Longair 2011), and as the energy of the gamma photon increases, the absorption effect becomes more noticeable. As a result, VHE photon flux is more attenuated than HE photon flux.
Furthermore, the density of the EBL increases significantly with redshift, and the probability of interaction with gamma photons rises consequently. During earlier cosmic epochs, the EBL was more intense particularly around the peak of star formation at $z \sim 2$ (Franceschini, Rodighiero, and Vaccari 2008).
As a result, the absorption effect depends both on the energy of the emitted photons and on the redshift at which they were emitted. The observed flux of gamma photons with energy E_γ, produced at a distance corresponding to redshift z, is given by:

$$\frac{dN_{obs}}{dE} = \frac{dN_{emi}}{dE} e^{-\tau(E_\gamma, z)}$$

where $\frac{dN_{obs}}{dE}$ is the observed flux, $\frac{dN_{emi}}{dE}$ is the emitted flux, and $\tau(E_\gamma, z)$ is the absorption factor.

The two plots reported in the figure 2.7 display how the optical depth of the EBL depends on both the energy of the gamma photons and the redshift of the sources.

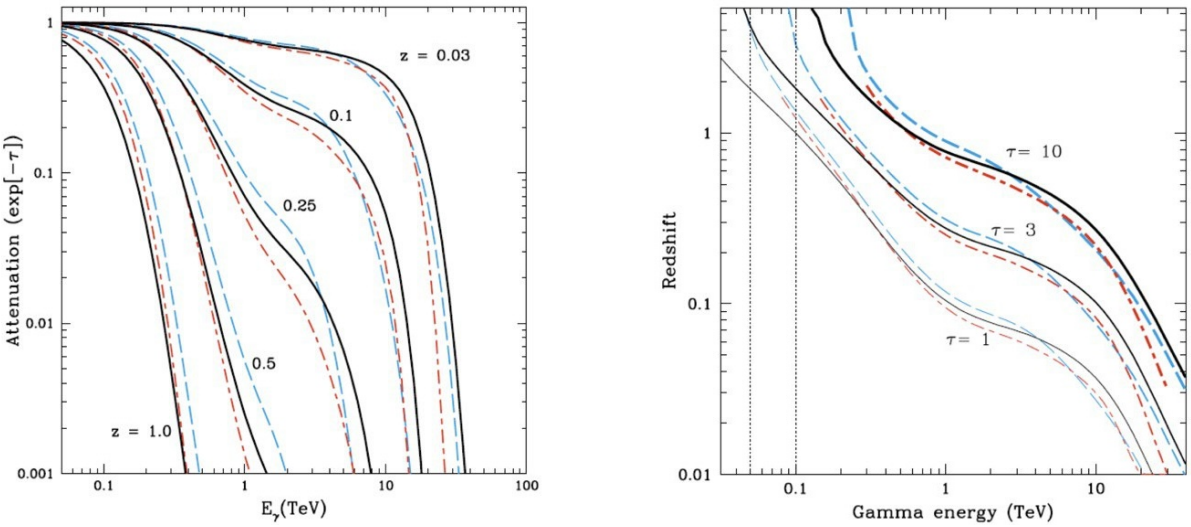

Figure 2.7: Left: Gamma-ray attenuation as a function of observed energy for sources at different redshifts. Right: Gamma Ray Attenuation Edge, showing the redshift at which the optical depth τ reaches values of 1, 3, and 10, as a function of the observed gamma-ray energy. From Primack et al. 2011

The left panel of Figure 2.7 shows the gamma-ray attenuation, expressed by the factor τ, as a function of the observed energy for sources at different redshifts. The curves indicate that in the VHE band ($E_\gamma > 100 GeV$), the attenuation due to the EBL increases with the gamma-ray photon energy and source redshift. For example, for gamma-ray photons with $E_\gamma = 1$ TeV, at lower redshifts (e.g., $z = 0.03$), the optical depth is very small ($\tau \sim 1$), meaning that these photons has experienced minimal attenuation. At higher redshifts (e.g., $z = 0.5$ or $z = 1$), the value of τ increases significantly, indicating that the photons has been strongly attenuated by the EBL. For a source at $z = 0.5$, the optical depth might be $\tau \approx 0.01$ for photons with $E_\gamma = 1$ TeV, implying that only a small fraction of the emitted photons at this energy have reached us. By knowing τ, we can reconstruct the intrinsic flux at the

time of emission by applying the correction factor e^{τ} to the observed flux.
The right panel of Figure 2.7 provides a different perspective by illustrating the Gamma Ray Attenuation Edge. This plot shows the redshift at which the optical depth τ reaches specific values (1, 3, and 10) as a function of the observed gamma-ray energy. The curves indicate how deeply we can observe into the universe at different energies before the gamma-ray photons become significantly attenuated. For instance, lower energy gamma rays (e.g., 0.1 TeV) can travel through the universe from sources at higher redshifts before reaching an optical depth of $\tau = 1$, whereas higher energy gamma rays (e.g., 1 TeV or above) are strongly attenuated at much lower redshifts. This means that as the photon energy increases, the distance we can observe decreases significantly.

2.2.1 Gamma instrumentation: direct and indirect measurement

Since the Earth's atmosphere is opaque to gamma photons, direct measurements can only be performed in the upper atmosphere using balloons, or in space using satellites. However, above approximately 100 GeV, the interactions with the atmosphere become so powerful that indirect detection is possible from the Earth's surface.

Satellities: the *Fermi*-LAT

Satellite-based gamma-ray detection directly observes gamma photons. Satellites are effective in the HE regime due to instrumental limitations. The technical challenges of transporting satellites into space require that their physical area be small, making it difficult to detect VHE photons, whose flux is too low to be easily detected with these limited areas.

The *Fermi* Gamma-ray Space Telescope (Atwood et al. 2009), launched by NASA in 2008, is a satellite designed to explore the HE universe. The satellite operates in a low Earth orbit at an altitude of approximately 565 km with an inclination of 25.6 degrees. It is equipped with two primary scientific instruments: the Large Area Telescope (LAT), a gamma-ray detector covering an energy range from 20 MeV to 300 GeV, and the Gamma-ray Burst Monitor (GBM), which operates at lower energies to monitor transient phenomena such as GRBs.

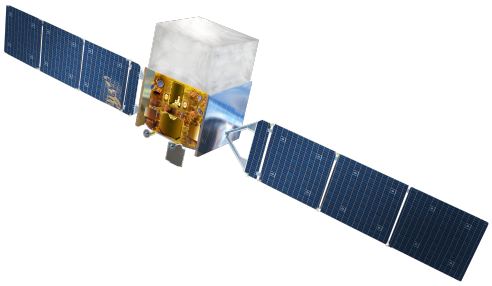

Figure 2.8: *Fermi* Gamma-ray Space Telescope

The *Fermi*-LAT's large field of view, approximately 2.4 steradians (~ 20% of the sky), allows scanning the entire sky every three hours, so it can detect transient phenomena like gamma-ray bursts and flares from blazars. The detector is composed of a tracker, consisting of multiple layers of silicon and tungsten, and a calorimeter made of cesium iodide (CsI) crystals acting as scintillators. The detection technique is pair production: when a high-energy gamma photon interacts with the tungsten, it converts into an electron-positron pair. The silicon strip detectors in the tracker capture the ionization paths of these particles, producing detectable charge signals. Beneath the tracker, the CsI crystal calorimeter measures the energy deposited by the electron-positron pair through scintillation

light, which correlates with the original gamma photon's energy, allowing for accurate energy measurement.

IACTs: MAGIC and CTAO

Imaging Atmospheric Cherenkov Telescopes (IACTs) are instruments used to detect gamma rays with energy above 100 GeV, and even lower with the upcoming CTAO. Because of the interaction with nuclei, when a VHE photon strikes the atmosphere, it produces a cascade of secondary particles known as an electromagnetic shower. This shower, typically develops at altitudes of 10-20 km above sea level, includes electrons and positrons traveling faster than the speed of light in air, generating Cherenkov light, which is a faint blue flash. This Cherenkov light has a duration of only a few nanoseconds and peaks in the blue-UV part of the spectrum. It is emitted with and angle θ_C given by $\cos\theta_C = 1/\beta n$, where β is the velocity of the particle divided by the speed of light (v/c), and n is the refractive index of the medium, that for the air is $n_a \approx 1.0003$. So for relativistic particles ($\beta \approx 1$) in atmosphere, the Cherenkov light is emitted in a cone with open angle of about $\theta_C \sim 1°$, illuminating an area of approximately $10^5 m^2$ on the ground. IACTs function by detecting these flashes of Cherenkov light. The telescopes are formed by a large reflective surface that reflects the Cherenkov light into a camera made up of photomultipliers. The captured image is then analyzed to reconstruct the direction and energy of the original gamma ray. The IACTs have an angular resolution of 0.1°, sufficient to precisely locate the sources in the sky, but they have a limited field of view and can only operate during dark, moonless nights, and under good weather conditions, reducing the total available annual observation time.

MAGIC

MAGIC [1] (Major Atmospheric Gamma Imaging Cherenkov) is a system of two IACTs located at an altitude of 2200 meters on the Canary Island of La Palma, at the Observatorio del Roque de los Muchachos (Sitarek et al. 2013). The first telescope, MAGIC-I, was completed in 2004. In 2009, a second telescope, MAGIC-II, was added to the observatory. The two telescopes are identical in design, each with a 17-meter diameter mirror. The addition of the second telescope enabled stereoscopic observations, which improved the reconstruction of the electromagnetic shower's direction and energy, thereby enhancing the angular resolution and sensitivity of the observations.

MAGIC telescopes are designed to detect VHE gamma rays in the range from 30 GeV to 100 TeV. The camera at the focal point of each telescope is composed of 1039 photomultiplier tubes (PMTs) arranged in a hexagonal pattern. These PMTs are highly sensitive to the faint light flashes generated by atmospheric showers and operate with fast electronics that allow for quick readouts.
The telescopes are operational during dark, moonless nights, which provides approximately 1,000 hours of observation time per year. However, observations are highly dependent on weather conditions, and operations can be disrupted by factors such as cloud cover, humidity, and wind, affecting the total available observational time.

[1] https://magic.mpp.mpg.de

Figure 2.9: The two MAGIC telescopes. Credits: Urs Leutenegger

CTAO

The Cherenkov Telescope Array Observatory [2] (CTAO) is planned as a global observatory. It will consist of two large arrays of telescopes located in the Northern and Southern Hemispheres, at La Palma in the Canary Islands and Paranal in Chile, respectively. This dual-site configuration will provide full-sky coverage, allowing CTAO to observe gamma-ray sources in both hemispheres. The two observatories will feature three types of telescopes, each optimized for different parts of the gamma-ray energy spectrum:

- *Large-Sized Telescopes (LSTs):* telescopes with a mirror diameter of about 23 meters, are designed to detect gamma rays at the lower end of the VHE spectrum (from 20 GeV to a few TeV). There will be four LSTs at each site.
- *Medium-Sized Telescopes (MSTs):* The MSTs have a mirror diameter of about 12 meters and are optimized for detecting gamma rays in the core energy range (between a few hundred GeV and a few tens of TeV). There will be about 25 MSTs at the southern site and 15 at the northern site.
- *Small-Sized Telescopes (SSTs):* These smaller telescopes, with a mirror diameter of about 4 meters, are designed to detect the highest energy gamma rays (above 10 TeV). Approximately 70 SSTs will be deployed at the southern site, where the focus will be on observing the central regions of the Milky Way.

CTAO will cover an energy range from 20 GeV to over 300 TeV, significantly extending the observable spectrum of gamma rays. This wide range allows it to explore both lower energy phenomena, typically missed by current IACTs, and the highest energy gamma rays, providing the most comprehensive view of the gamma-ray universe. The dual-site configuration allows for continuous monitoring of the sky, ensuring that even when one site is unavailable due to daylight or weather conditions, the other site can perform observations. The annual observational time at each site will be around 1400 hours. Compared to MAGIC and other IACTs, CTA will offer approximately ten times greater sensitivity across its energy range.

[2] https://www.ctao.org

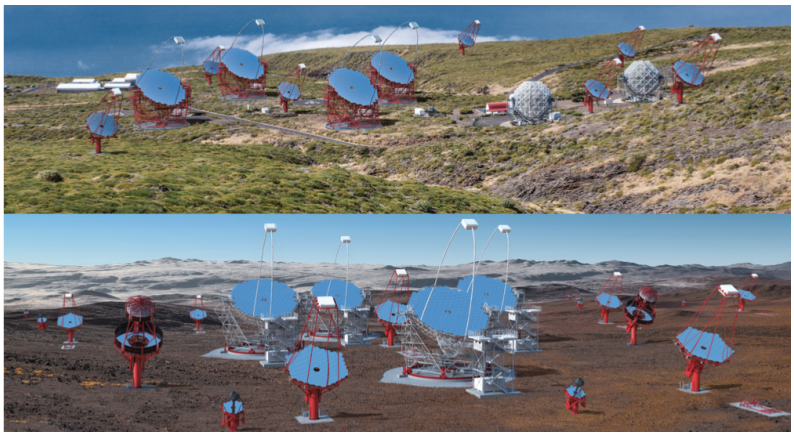

Figure 2.10: Renderings of CTA observatories. Upper illustration: CTA-North; credit: Grabriel Pérez Díaz, IAC. Lower illustration: CTA-South; credit: Gabriel Pérez Díaz, IAC / Marc-André Besel, CTAO.

Other IACTs

- **H.E.S.S** (High Energy Stereoscopic System)[3] is a system of five IACTs located in the Khomas Highlands of Namibia, at an altitude of 1800 meters. The array began operations in 2002 with four telescopes, each with a 12-meter diameter mirror. In 2012, a fifth telescope, **H.E.S.S. II**, was added at the center of the array, featuring a much larger 28-meter diameter mirror, which significantly improves the system's sensitivity, especially at lower energies around 30 GeV. H.E.S.S. is designed to detect VHE gamma rays in the energy range from 30 GeV to tens of TeV.

- **VERITAS** (Very Energetic Radiation Imaging Telescope Array System)[4] is an array of four IACTs located at the Fred Lawrence Whipple Observatory in southern Arizona, at an altitude of 1268 meters. The telescopes began operations in 2007, each equipped with a 12-meter diameter mirror. The array is optimized to detect gamma rays in the energy range from 85 GeV to over 30 TeV.

2.3 Multi-wavelenght data and SED costruction

As mentioned at the beginning of the section 2.2, constructing a complete picture of a blazar is challenging, as it requires combining observations from different instruments across the wide range of wavelengths of blazars' emission. The variability further complicates the process of computing and analyzing multi-wavelength emission datasets, as constructing SED models requires contemporaneous data. However, to study the mean behavior of a blazar, the shape of the SED can be constructed using averaged data from different activity states. In this way, a mean SED can be obtained. Thus, the study of data accumulated over the years provides a historical perspective, allowing to track the long-term behavior of blazars and build and test average SED models. By comparing historical datasets with new observations, it becomes possible to test evolutionary models and identify correlations and patterns that might not be apparent from isolated observations. In this context, astronomical catalogs are fundamental for the study of blazars, as is organizing them in formats that make data easily

[3] https://www.mpi-hd.mpg.de/hfm/HESS/
[4] https://veritas.sao.arizona.edu

accessible and facilitate analysis. Often made public by scientific collaborations, these catalogs are essential for conducting multi-wavelength studies on large samples of sources, correlating observations in different bands.

DL5 MAGIC data portal

In the specific case of TeV observations, the development of the **DL5 MAGIC Data Portal** aims to systematize data from past observations published by the MAGIC collaboration (Doro et al. 2019). At the moment, there is no catalog that compiles the observational data obtained by MAGIC. The DL5 MAGIC Data Portal, developed by the MAGIC collaboration with support from the Port d'Informació Científica (PIC) in Barcelona, organizes high-level data related to MAGIC collaboration publications. This portal includes gamma-ray data and multi-wavelength observations data used in the publications to produce scientific outputs like SEDs and light curves.
Each paper has a dedicated folder within the portal, that stores both data and metadata relevant to the publication. The observational data are stored in the .ecsv format. These files contain detailed information about each observation, including source names, energy ranges, flux measurements, uncertainties, observation times, and the instruments used. Each .ecsv file corresponds to specific figures in the paper, which are referenced directly in the metadata.
In addition to the data, each folder contains a .yaml file that serves as the metadata repository, providing an overview of the paper and its associated scientific content. The .yaml file includes details, such as the title of the paper, author list, journal references, DOI, and arXiv links. It also lists all the target sources in the dataset and provides a list of all the .ecsv files related to the publication, linking them to specific figures in the paper, making it easy to navigate between the scientific output and the raw data.
This setup facilitates easy access to fully processed data, enabling researchers to focus on analysis rather than data preparation. The project goal is to streamline data sharing within the scientific community and store past observational data in the TeV band. The creation of the MAGIC Data Portal will provide not only a centralized resource for gamma-ray observations, but also setting the stage for future developments in the field.

The ability to easily connect past and present data across various wavelengths enhances the planning and execution of observational campaigns for future projects like the CTAO. With this comprehensive data foundation, CTAO can more efficiently target relevant events, such as recurring blazar flares, and prioritize the most promising sources. Furthermore, the DL5 format's standardized approach to data storage and accessibility serves as a model for CTAO's own data management strategies. This ensures that the data of CTAO remain interoperable with existing datasets, allowing for easy integration of new observations with historical data. This integration enables a more comprehensive analysis of the observed phenomena, building on decades of research to produce deeper insights into the high-energy universe.

Throughout my thesis work, I contributed to the project by formatting publicly released data into .ecsv format for SEDs and light curves from various MAGIC collaboration publications on blazar observations.

Markarian Multiwavelength Data Center

In addition to gathering and systematizing data from past observations, it is necessary to manage the large volume of information. For this purpose, astronomical portals that provide access to public catalogs and utilize specialized tools for data collection and analysis are very helpful for studies on large samples. A powerful example is the **Markarian Multiwavelength Data Center** (MMDC) [5]. It is a specialized online platform designed to support researchers studying blazars and other AGNs. It provides access to a broad range of multiwavelength data collected from different telescopes and observatories. MMDC allows users to construct the SED of an object using the available data, but also offers the option to upload personal datasets and build an SED model for those data using both Synchrotron Self-Compton (SSC) (Bégué et al. 2024) and External Compton (EC) models (Sahakyan et al. 2024).
MMDC provides a highly customizable interface. It is possible to use a Time Filtering feature for select specific time intervals to filter the observational data, allowing for the analysis of data over specific periods, which is particularly useful for studying the variability of blazar emissions. The interface also enables users to choose which instruments and catalogs to include in the analysis, offering flexibility in the analysis.
The platform integrates powerful computational tools such as Convolutional Neural Networks (CNNs) to facilitate the modeling of radiative processes in blazars. These tools significantly reduce the computational time needed to simulate emissions, allowing for rapid exploration of parameter spaces when building SED models.

Firmamento: A General Package for Multi-Messenger Astronomy

Another platform that aids in managing and analyzing large datasets across different wavelengths is Firmamento (Tripathi et al. 2024), used in this thesis to extract the parameters for the analysis. Firmamento is an online platform designed for both citizen and professional researchers to study multifrequency sources, particularly blazars, which emit across the entire electromagnetic spectrum. It offers access to tables of blazar candidates compiled through various criteria, lists of other types of multi-wavelength emitters and a catalog of known blazars, including over 6400 objects that will be periodically updated with newly published blazars. It joins numerous tools and huge data sets into a comprehensive approach to analyzing characteristics of blazars in the general framework of multi-messenger astrophysics. Firmamento utilizes the Aladin software to visualize the target, the VOU-Blazars tool to generate SEDs and integrate BlaST (Blazar Synchrotron peak Locator), a machine learning tool developed to estimate the position ν_{sync} of the synchrotron peak.

Aladin [6] is an interactive sky atlas, created in 1999, that allows users to explore digitized astronomical images obtained at different wavelengths, overlay data from several databases, such as Simbad or VizieR, and interactively compare different datasets for specific areas of the sky (Bonnarel et al. 2000). In Firmamento, Aladin provides access to a comprehensive selection of high-quality surveys across radio, infrared, optical, X-ray, and gamma-ray energies, which are particularly useful for blazar identification.

[5] https://mmdc.am
[6] http://aladin.cds.unistra.fr

VOU-Blazars (Chang, Brandt, and P. Giommi 2020) is specifically designed for searching and studying blazars by building fine-grained SEDs using more than 90 existing catalogs and spectral databases available through *Virtual Observatories* (VO). The selection of blazar candidates was made by adopting a two-step procedure. The first step is the source identification: VOU-Blazars provides access to the data using VO cone search pipelines to targeted catalogs containing photometric data in at least the radio and X-ray bands. The second one is the construction of SED: the tool collects data from other catalogs covering frequencies from radio to TeV bands, providing a multi-wavelength view of each blazar candidate. After that, VOU-Blazars plots the SED for each candidate and corrects for Galactic extinction where required, because blazars are extragalactic sources and their observed flux can be affected by dust within the Milky Way. This dust scatters and absorbs radiation, primarily in the UV and optical bands, heating up and then re-emitting it in the infrared as thermal emission. Without correcting for Galactic extinction, the intrinsic emission from the blazar could be underestimated at shorter wavelengths, leading to inaccurate flux measurements and a misinterpretation of the SED. It also generates error circle maps, integrated into the Aladin visualizer, that show the positional uncertainties of detections at various wavelengths, allowing for precise localization. This aspect is very useful when multiple sources fall within the same region of uncertainty, as it helps to identify the most likely blazar counterpart by visualizing overlaps and positional errors across different bands. This combination of multi-wavelength SED construction and error region mapping ensures both accurate identification and thorough analysis of each blazar candidate.

BlaST, the Blazar Synchrotron Peak Locator (Glauch, Kerscher, and Paolo Giommi 2022), is designed to estimate the position of the synchrotron peak in blazar SEDs using machine learning techniques. It takes the SED data produced by VOU-Blazars as input. Using a highly-developed machine learning algorithms allows the tool to analyze the SED and determine the frequency of the synchrotron peak, as well as its flux. This is done by training models on known blazars data to recognize patterns and make accurate predictions. This kind of estimate will be more accurate because of the iterative refinement and validation against the known blazar samples.

Chapter 3

Methodology

The present work aims to compare observations of blazars made in the GeV band by the *Fermi*-LAT satellite with those made in the TeV band by ground-based IACTs, in order to characterize the distinct populations observed at these different energy ranges. As discussed in the previous chapter (see section 2.1), blazars emit across the entire electromagnetic spectrum, but the position of the two peaks in their SED and their luminosity vary significantly. Moreover, observations in the gamma-ray range require different techniques and instruments, resulting in two distinct populations in the GeV and TeV bands. To this end, two samples were considered: one comprising blazars detected by MAGIC, H.E.S.S., and VERITAS at TeV energies, and another consisting of blazars detected by *Fermi*-LAT at GeV energies.
The comparison will focus on three key parameters: the redshift, which indicates how far observations can reach and highlights cosmological constraints; the synchrotron peak frequency, and the synchrotron peak flux, both of which serve as proxies for the frequency and flux of the IC peak, respectively.
This chapter describes the process used to construct the two samples and outlines how the relevant parameters were extracted for comparison between the two populations.

3.1 GeV sample

For the GeV sample, the **4FGL-DR4** catalog (Ballet et al. 2024) was considered. It contains 7194 gamma sources observed by *Fermi*-LAT during the first 14 years of activity. Among them, were selected the blazars identified by a working group I am part of, coordinated by Paolo Giommi and including many members from the University of Padua. The group analyzed the *Fermi*-LAT 4FGL-DR4 catalog using Firmamento (see section 2.3) to identify blazars among the gamma-ray sources contained in the catalog. Of the 7194 total sources, only the 5060 sources with galactic latitude $|b| > 10$ were considered, in order to exclude the Galactic Plane, which contains significant diffuse gamma-ray emission primarily produced by interactions between cosmic rays and the interstellar medium, potentially obscuring extragalactic sources such as blazars. The partial results of this work were used in this thesis to form the GeV sample, with **2238 associated blazars**.
The association of a blazar with a gamma-ray signal is not straightforward, as it requires, in addition to obvious observational challenges, a comprehensive analysis of the emission across different wavelenghts. The analysis conducted by Giommi's group aimed to test the *Fermi*-LAT associations

by independently reanalyzing the 4FGL-DR4 using Firmamento. The association process performed using Firmamento is described step-by-step in the next section 3.1.1.

3.1.1 Association

To proceed with the association, in addition to the table of 5060 sources from the 4FGL-DR4 catalog with $|b| > 10$, the Fermi-LAT error circle, defined by the orientation and the major and minor axes of the error ellipse, is provided as input to Firmamento. This allows for the association of gamma-ray sources identified by the *Fermi*-LAT satellite, taking into account the positional uncertainties of the observations. The portal uses VOU-Blazars (2.3) to search through all available catalogs, finding data within the sky region around the detected gamma signal and inside or near the boundary of the *Fermi*-LAT error circle, in order to identify counterparts at other wavelengths. A sky map with RA and DEC is displayed (upper left in Figure 3.1), showing the *Fermi*-LAT error circle for the position, along with the various sources detected in that region of the sky. Additionally, the sky region is visualized using Aladin, displaying the sources outlined by the error circles for all the wavelength in different colors (on the right in 3.1). These sources are all potential candidates for association with the gamma-ray signal detected by *Fermi*-LAT. The portal lists the candidates, providing a possible classification for each source (Blazar, Pulsar, Nova, etc.). It is useful to explore the sky region images across the different available bands to see what is displayed and to determine if multiple nearby candidates are actually the same object falling within that error circle. After choosing the best candidates, the SED is plotted to check its shape and the consistency of the data with a blazar identification (figure 3.2. Along with the SED, the portal uses BlaST (see 2.3) to provide the position of the synchrotron peak $\log \nu_p$ and the corresponding flux $\log \nu F_\nu$, also plotting the position with a yellow dotted line on the SED.

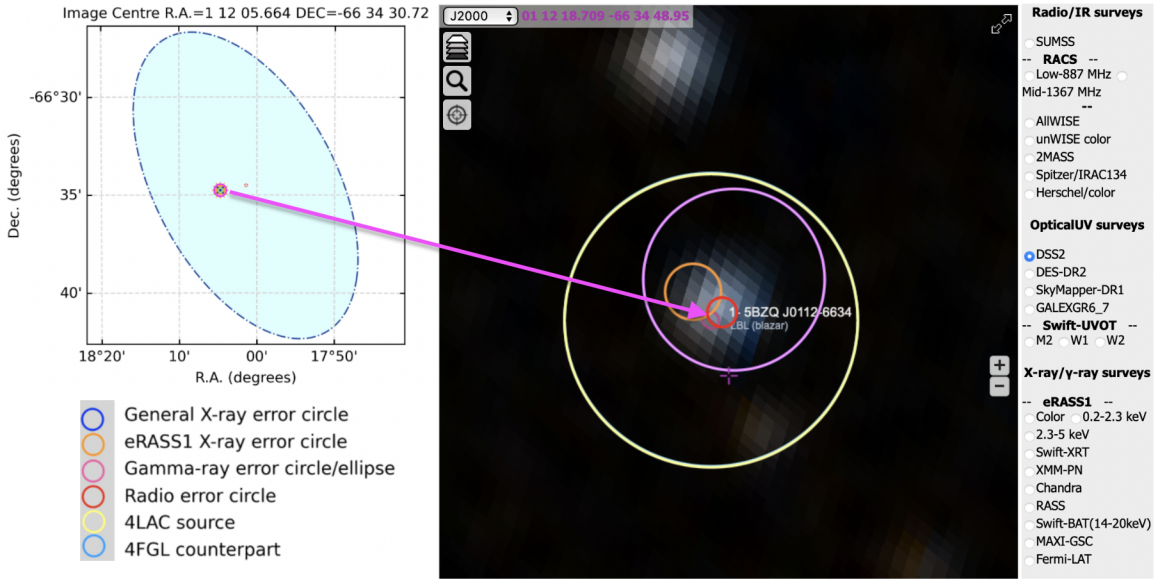

Figure 3.1: Firmamento output for 4FGL J0112.0-6634, case of agreement. Upper left: sky map with position error circle, along with the possible counterparts. Lower left: the legend of the error circle. On the right: the Aladin sky region with the error circle surrounding the candidate.

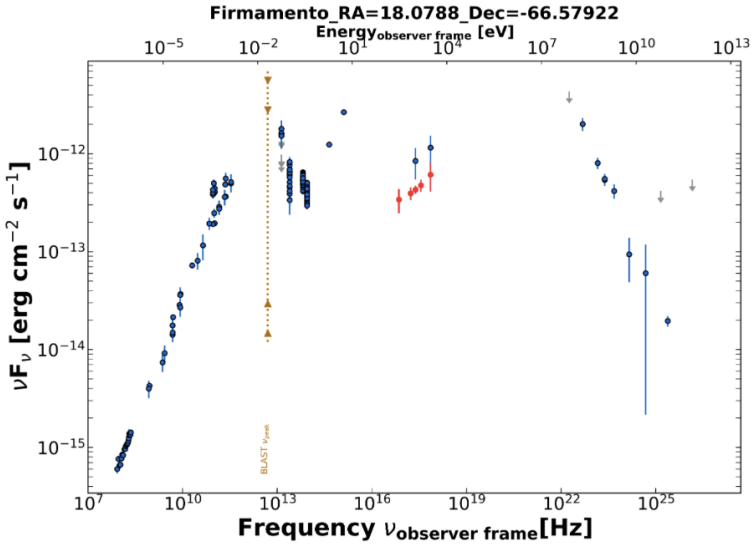

Figure 3.2: SED of 4FGL J0112.0-6634 plotted by Firmamento.

The work is now complete, and a paper is in preparation to present the results. A summary of the association is reported in Figure 3.3. The results are in agreement with the associations made by the *Fermi*-LAT collaboration in 84.3% of the cases. Among these cases, 3338 blazar associations were made with the same candidate as in the 4FGL catalog, and for 841 sources, the absence of a blazar candidate was confirmed. The disagreement with the 4FGL associations amounts to 12.9%. Among these, there are 209 blazar associations with a different candidate, and, very interesting for future observation, a total of 430 new blazar associations for previously unassociated sources. An example of a new association is reported in Figure 3.4.

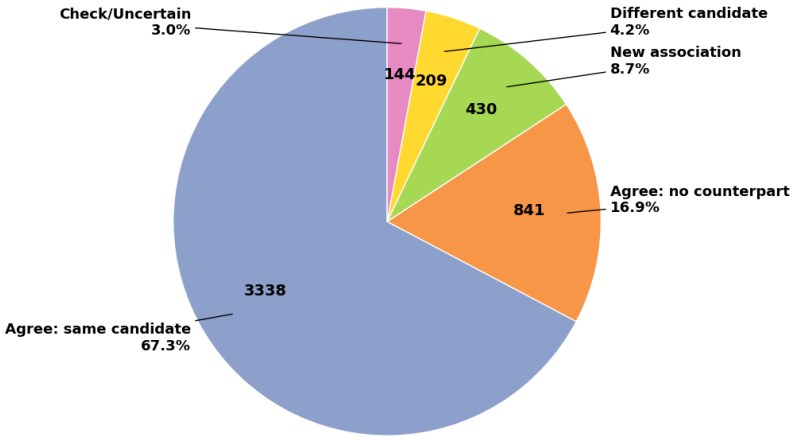

Figure 3.3: Final results for the analysis of the 4FGL-DR4 catalog performed using Firmamento.

The association is not clear in all cases. During our work, we encountered many ambiguous situations in which it was not possible to identify the counterpart, so there is a 3% of uncertain associations that will need to be better evaluated in the future. However, the percentage of agreement with the associations performed by the *Fermi*-LAT collaboration confirms the reliability of the results obtained by Giommi's group, ad used in this thesis.

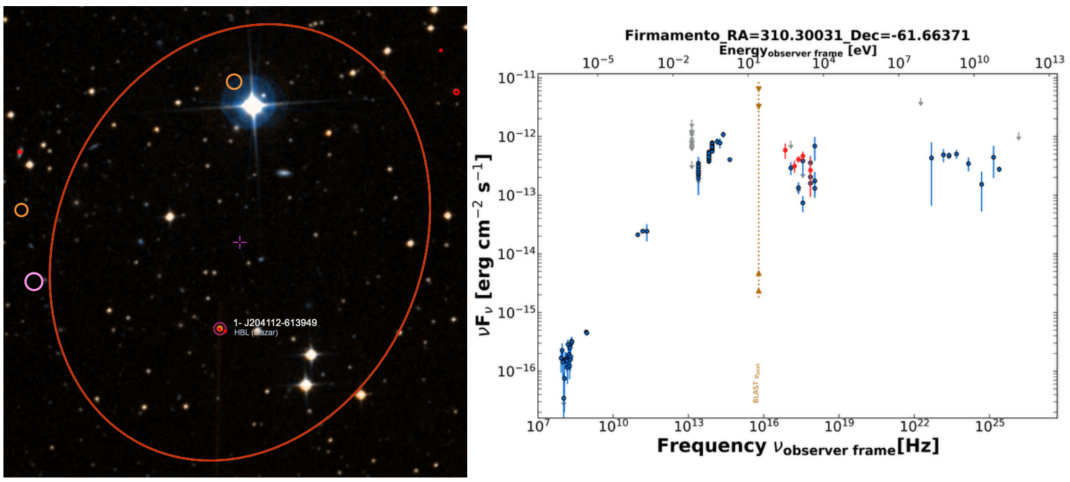

Figure 3.4: Firmamento output for the 4FGL J2041.1-6138 source unassociated in 4FGL-DR4. Firmamento found a counterpart (left) with a SED consistent with a blazar association (right).

3.2 TeV sample

The TeV sample was compiled by selecting blazars that had been observed by IACTs listed in the TeVCat 2.0 and STeVCat, resulting in a total of **86 blazars**. In Table A.2, there is the complete list of TeV-detected blazars observed by MAGIC, H.E.S.S. and VERITAS.

TeVCat 2.0 *(TeV Catalog)* [1] is an online catalog managed by Scott Wakely and Deirdre Horan. It contains 334 TeV objects, both galactic and extragalactic, of which 85 are blazars. The catalog provides observed and derived parameters along with notes from the instruments that observed each source and links to the relative publications, information that was used during the analysis to characterize the properties of TeV sources. A map of the sky with all the objects from the TeVCat catalog, superimposed to the *Fermi*-LAT full sky map, is shown in the Figure 3.6

STeVCat *(Spectral TeV Extragalactic Catalog)* (Gréaux et al. 2023) consists of extragalactic TeV sources and was developed to compile and standardize the high-level results of very-high energy observations from IACTs telescopes. It systematizes published spectra and metadata from 73 sources, of which 59 are blazars, observed from 1992 to 2021, into a unified format, and provides a table of all these sources with information such as RA, DEC, and redshift, along with references to the relevant publications. The versatility of the format allows for efficient loading and analysis using tools like GammaPy (Donath et al. 2023). A map of the sky with all the objects from the STeVCat catalog is reported in Figure 3.5.

[1] http://tevcat2.uchicago.edu/
[2] From http://tevcat2.uchicago.edu

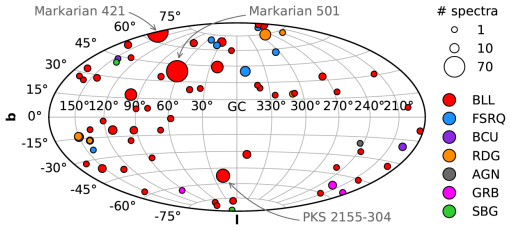

Figure 3.5: STeVCat object sky map in galactic coordinates. The source type is color coded. From (Gréaux et al. 2023).

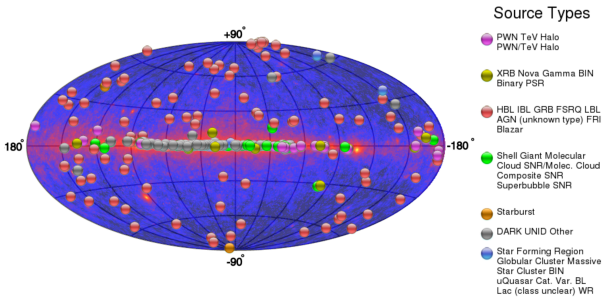

Figure 3.6: TeVCat object sky map in galactic coordinates, superimposed to the *Fermi*-LAT full sky map. The source type is reported in the legend.[2]

3.3 Parameters and Classification

For 77 of the TeV blazars observed by IACTs, the **redshift** measurements were obtained from specific publications referenced in TeVCat and STeVCat. For those whose redshift was not available in these catalogs, it was instead extracted from the NASA/IPAC Extragalactic Database (NED)[3]. In the same way, for GeV blazars redshift values are taken from the 4FGL-DR4 catalog when available; otherwise, redshift values from the NED are used. Redshift is available for 1807 sources in the GeV sample.

The **synchrotron peak** frequency ν_p and its corresponding **flux** νF_ν, were obtained using *BlaST* integrated within Firmamento (see section 2.3). During the work with Giommi's group, after a blazar was identified and its SED plotted, the parameters were extracted for each identified blazar.
For the 86 TeV blazars, I followed the same procedure to obtain the parameters BlaST in Firmamento.

3.3.1 Blazar SED Type Classificationn

The classification of an object in the subclasses LBL, IBL and HBL exposed in section 2.1 is not univocal in the catalogs and can change from one observation to another, because of the variability of the sources and the choice made to classifying them. Thus, during this work the division into subclasses is based on the value of ν_p extracted with Firmamento, as follows:

- $\nu_p \leq 10^{13.5}$ Hz $\Rightarrow$ LBL+FSRQ
- $10^{13.5} < \nu_p \leq 10^{15}$ Hz $\Rightarrow$ IBL
- $\nu_p > 10^{15}$ Hz $\Rightarrow$ HBL

FSRQs were grouped with LBLs due to key similarities in their SEDs, with synchrotron emission peaking in the infrared to sub-millimeter range and inverse Compton emission at GeV energies in both cases. These shared characteristics in energy distribution suggest that FSRQs and LBLs can be classified together, particularly when considering a classification that disregards luminosity and emission lines, as in this thesis.

[3] https://ned.ipac.caltech.edu

Classifying blazars based on the frequency of the synchrotron peak ν_p is useful because it is directly observable from the SED and provides as a proxy for the whole SED, as already said in section 2.1. This classification is not only an observational distinction but also reflects the physical conditions inside the blazar jet, as ν_p is a physical parameter that mirrors the maximum energy of the relativistic electron population and the strength of the magnetic field.
Thus, blazars with higher synchrotron peak frequencies, like HBLs, have more energetic electron populations, which, in turn, causes their inverse compton peaks to shift to higher energies, typically in the TeV range. On the other hand, blazars with lower synchrotron peaks, like LBLs, are characterized by lower-energy electrons, leading to emission at lower frequencies, with the IC component typically found in the GeV range.

The parameter νF_ν represents the energy observed at the synchrotron peak frequency. While it doesn't directly reflect the total energy output without accounting for cosmological corrections, in this thesis the primary focus is on comparing the blazar populations observed by IACTs and *Fermi*-LAT. Here, νF_ν serves as an indicator of the flux range at which these blazars are observable, which is key to understanding the visibility of the populations in the GeV and TeV bands.

Chapter 4

Analysis and Results

This chapter presents a comparative study of the blazar populations observed in the TeV and GeV bands by the IACTs MAGIC, VERITAS, H.E.S.S. and the *Fermi*-LAT telescopes, respectively. First, the synchrotron peak position ν_p distribution will be examined to determine the SED type classifications within both populations. Then, the redshift and synchrotron peak flux distributions will be analyzed to explore the distinct characteristics of the blazars in each population. Finally, the distribution of the flux at the synctrotron peak νF_ν will be considered. In the last section, a comparison between blazars detected in the TeV and GeV bands is presented, with a focus on future observations by CTAO.

4.1 Synchrotron peak position

By considering the distribution of the synchrotron peak position, it becomes evident that the two instruments are sensitive to different blazar populations. Figure 4.1 shows the two distributions.

IACTs: the left plot in 4.1 shows a concentration of blazars with synchrotron peaks between $\nu_p = 10^{15}$ Hz and $\nu_p = 10^{18}$ Hz, indicating that IACTs tends to observe HBLs (71% of the total TeV-detected blazars), with only a small fraction of IBLs and LBLs present.

***Fermi*-LAT**: in the right plot in 4.1, it is clear that *Fermi*-LAT detects blazars with a wider range of synchrotron peak frequency, with a larger proportion of blazars having lower synchrotron peak frequencies, particularly between $\nu_p = 10^{12}$ Hz and $\nu_p = 10^{14}$ Hz. This indicates that *Fermi*-LAT observes a more diverse population of blazars, with most of them being IBL and LBLs+FSRQ (65.3%).

The difference in the types of blazars observed by IACTs and *Fermi*-LAT is due to the flux sensitivities of the two instruments. *Fermi*-LAT is less sensitive to lower fluxes compared to IACTs. Therefore, since HBLs are intrinsically less luminous than IBLs, LBLs, and FSRQs, they have weaker fluxes and are more difficult for *Fermi*-LAT to detect, which tends to favor LBLs and FSRQs. On the other hand, IACTs are sensitive to lower flux levels and can thus detect HBLs, which also have high-energy emissions at higher frequencies.

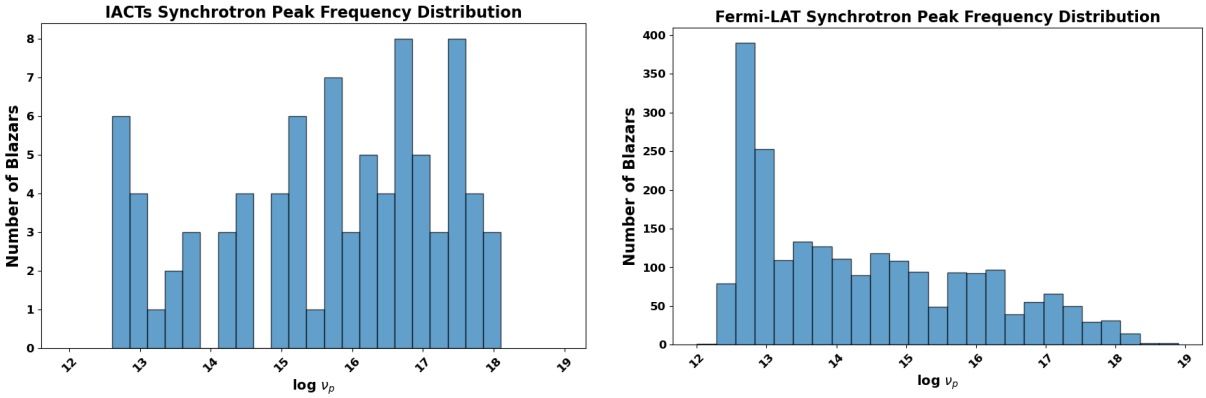

Figure 4.1: Left: IACTs $\log \nu_p$ distribution. Right: *Fermi*-LAT $\log \nu_p$ distribution

Thus, the two instruments observe two different blazar populations, with IACTs primarily observing HBLs, while *Fermi*-LAT captures a broader range of SED types, predominantly IBLs and LBLs. Table 4.1 gives an overview of the total number of blazars in each sample, broken down by SED type and the number of sources with known redshift.

	Total Number	**HBL**	**IBL**	**LBL+FSRQ**	**z known**
***Fermi*-LAT**	2238	777 (35%)	485 (21%)	970 (44%)	1807
IACTs	86	61 (71%)	13 (15%)	12 (14%)	86

Table 4.1: Summary of: number of blazars in the two sample; number of blazar for each SED type; number of blazars with known redshift.

In the following section 4.2, the redshift distribution of both samples will be analyzed to further characterize the two populations.

4.2 Redshift distribution

In this section, the redshift distribution of the two samples will be analyzed, and the differences between them will be discussed and justified.

IACTs: the redshift distribution, as shown on the left in Figure 4.2, is strongly concentrated at low redshifts, with 61 blazar observed at $z < 0.3$ out of a total of 85 blazars. After this initial peak, there is a significant decrease in the number of detected blazars, with a smaller number of sources distributed between $z = 0.3$ and $z = 0.6$ and no sources after $z = 1$.
The cumulative redshift distribution, on the right in Figure 4.2, reflects this trend. The curve rises rapidly at low redshifts, with the most of the blazars detected below $z = 0.3$. Beyond this point, the cumulative curve flattens, indicating a lower detection rate.

***Fermi*-LAT**: as shown in the left panel in Figure 4.3, the distribution spans a broader and distributed range. While there is a noticeable concentration of blazars below $z = 0.5$, *Fermi*-LAT continues to detect a significant number of sources beyond this, with the distribution extending up to $z = 3.5$. The presence of blazars even at these high redshifts highlights *Fermi*-LAT's capability to ob-

serve distant sources. The cumulative redshift distribution shown in the right panel in Figure 4.3 confirms this trend, with a steady and gradual rise up to $z = 3.5$. The curve flattens beyond $z = 2$, suggesting that high-redshift blazars become rarer or more difficult to detect, yet *Fermi*-LAT still captures a portion of these distant sources[1].

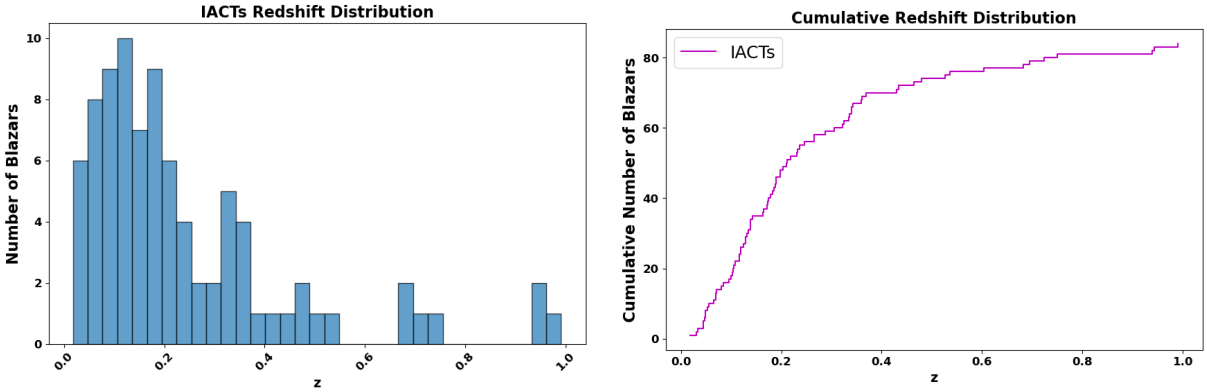

Figure 4.2: Left: IACTs z distribution; Right: IACT cumulative z distribution

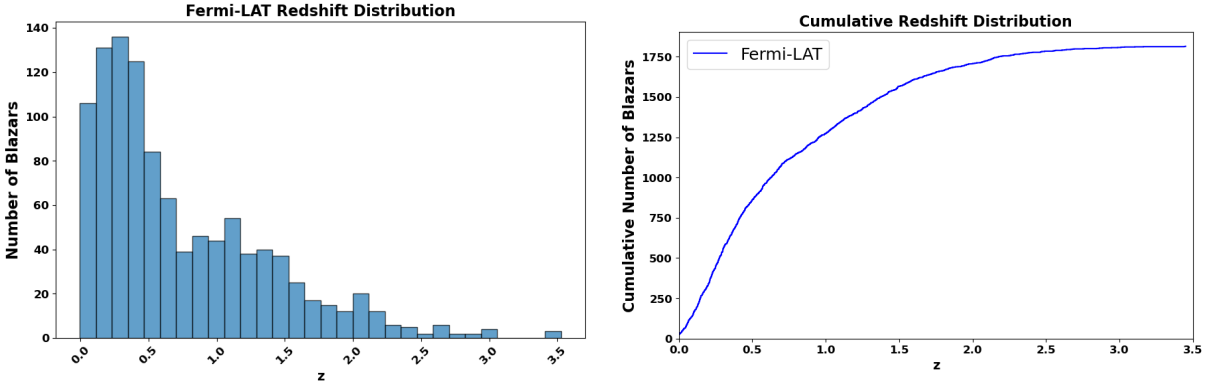

Figure 4.3: Left: *Fermi*-LAT z distribution; Right: *Fermi*-LAT z cumulative distribution

In the comparative cumulative percentage distribution shown in Figure 4.4, the differences between IACTs and *Fermi*-LAT are evident. The IACTs curve shows a rapid rise, with 50% of the detected blazars located below $z = 0.15$ and almost 80% of the sources concentrated below $z = 0.3$. The *Fermi*-LAT curve rises more gradually. At $z = 0.3$, only about 35% of the total blazars have been detected, versus IACT's 80%. The *Fermi*-LAT curve continues to increase steadily, reaching 50% at approximately $z = 0.7$ and gradually approaching 100% at $z = 3.5$.
This shows that *Fermi*-LAT detects blazars over a much wider redshift range compared to IACT, with a more even distribution of sources across both low and high redshifts.

The observed differences in redshift distribution can be attributed to several interrelated factors. First, as redshift increases, the density of the **Extragalactic Background Light** (EBL) encountered by photons rises, and the interaction between EBL and gamma photons through pair production

[1] For visualization purposes, have been excluded from all the *Fermi*-LAT plots the two sources detected beyond $z = 3.5$: 4FGL J1510.1+5702 with $z = 4.313$ and 4FGL J1233.7-0144 with $z = 6.395203$.

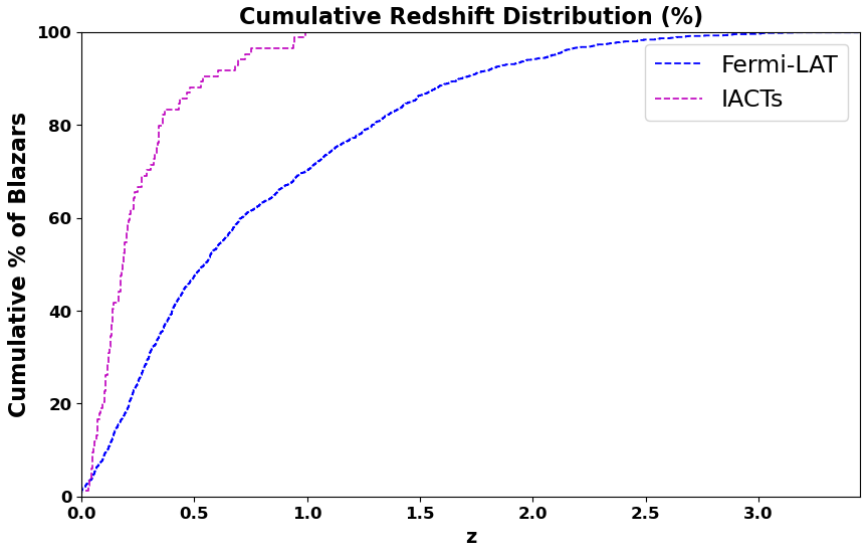

Figure 4.4: Cumulative percentage z distribution of the blazars observed by IACTs and *Fermi*-LAT.

becomes more significant, effectively absorbing the gamma rays. VHE photons are more likely to be absorbed (see 2.2), further limiting the observable flux from high-redshift blazars in the TeV range. This creates a selection bias in IACTs, which are primarily sensitive to VHE photons and thus mainly detect nearby blazars. The *Fermi*-LAT telescope is primarily sensitive to HE photons, for which the EBL effect is less important, allowing it to observe blazars at higher redshifts.

Then, according to the **blazar sequence** (see 2.1), HBLs are intrinsically less luminous than IBLs and LBLs. This lower luminosity results in weaker fluxes, making HBLs harder to detect, particularly at higher redshifts where flux attenuation is even more important due to EBL absorption. The intrinsic brightness allows LBLs and FSRQs to be detected even at greater distances.

Another important observational bias arises from the difference in the time response of the instruments. The Figure 4.5 compares the **differential flux sensitivity** of *Fermi*-LAT and CTAO as a function of time for different energy values. The plot shows that *Fermi*-LAT has a higher minimum detectable flux compared to CTAO for the same integration time, regardless of the energy considered. IACTs like CTAO are capable of detecting much lower fluxes in shorter time intervals. This is related to the effective area of the two instruments. The effective area of ground-based IACTs is significantly larger compared to *Fermi*-LAT. In fact, the Cherenkov light cone, triggered by the electromagnetic shower, covers a large area on the ground, typically around $10^5 m^2$ (see 2.2.1). This effectively increases the detection area of IACTs far beyond the physical size of the telescope. Therefore, IACTs needs a shorter integration time to observe lower flux, and can observe short-lived events such as blazar flares. On the other hand, *Fermi*-LAT detection area is limited to the physical area of the detector, meaning it must detect the direct photons that hit the detector. The area is approximately $1 m^2$, resulting in a lower photon-collecting capability, which necessitates longer integration times. This may cause it to miss these rapid transients events. As a result, IACTs tend to detect flares from high-redshift blazars and miss the baseline emission in the quiescent state, leading to an overrepresentation of flaring sources at higher redshifts. Conversely, *Fermi*-LAT's broader energy coverage allows it to detect non-flaring blazars at higher redshifts, providing a more comprehensive sample

that is less dependent on the blazar's activity state.
These effects introduce a detection bias, and approximately for $z > 0.5$, blazars can be detected by IACTs only in the state of flares.

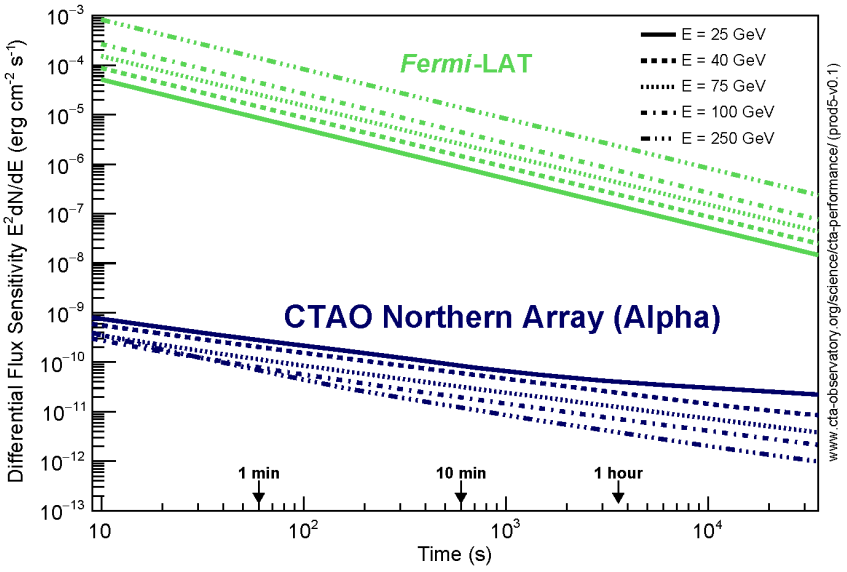

Figure 4.5: Differential flux sensitivity as a function of time comparison for *Fermi*-LAT e CTAO.[2]

Therefore, this combination of factors results in a different redshift distribution for blazars detected in the TeV and GeV energy ranges. The differences in the detectability limits by distance become more evident when considering the SED type of the sources that make up the two samples, as follows.

Redshift distribution by SED type

The redshift histograms by SED type for the GeV and TeV samples are shown in Figures 4.6, with columns color-coded by blazar SED type. The total height of each column represents the total number of blazars at that redshift. The colored segments within each column indicate the number of blazars belonging to each specific class.

IACTs: the IACTs sample shows HBL dominance at lower redshifts, but their numbers decline sharply beyond $z = 0.3$, with just one HBL detected above $z = 0.5$ [3]. At higher redshift are most commonly observed the LBLs and FSRQs. The only two blazars detected above $z = 0.8$ are PKS 1441+25 ($z = 0.939$) and S3 0218+35 ($z = 0.944$), both classified as FSRQs in TeVCat, and therefore intrinsically highly luminous. According to the TeVCat catalog, PKS 1441+25 was detected by MAGIC during a period when the source entered an exceptionally high state across optical, X-ray, and gamma-ray frequencies, making its detection possible due to the intense flare during that time. For the blazar S3 0218+357, TeVCat reports that it is a gravitationally lensed blazar, and the lensing effect amplifies the brightness of the source, allowing it to be detected despite its high redshift compared to other blazars

[2] From https://www.ctao.org
[3] Note that for these blazar RGB J0136+391, the redshift was obtained from NED since it was not available in the TeV catalogs, and it may not be accurate.

in the TeV sample.

***Fermi*-LAT**: up to $z < 0.5$, HBLs dominate, but their numbers decrease quickly as redshift increases, with very few detected above $z = 1$. After this, LBLs become the main population. IBLs are more often observed at lower redshifts but decline more gradually than HBLs, with some detected at intermediate redshifts ($z \sim 1-2$).

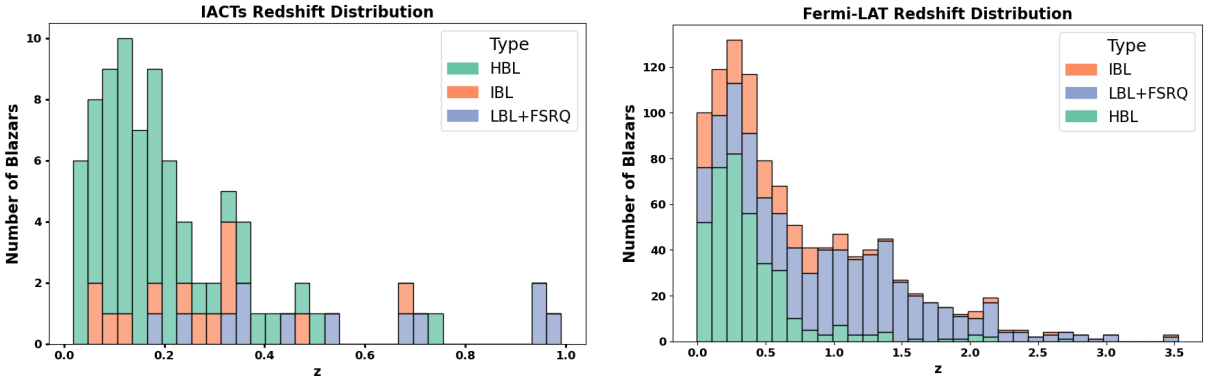

Figure 4.6: Left: IACTs z distribution color-coded by blazar type; Right: *Fermi*-LAT z distribution color-coded by blazar type

The IACTs sample is biased by the dominance of HBLs, while the *Fermi*-LAT sample includes a significant number of LBLs and IBLs at higher redshifts, providing a more complete view of the redshift trend in relation to SED type. However, the two distributions are consistent. At low redshifts, both instruments exhibit a similar pattern, with HBLs initially predominating and then shifting to LBLs. This shift occurs more rapidly in the IACTs sample, whereas *Fermi*-LAT continues to detect HBLs up to $z = 0.5$, after which IBLs and LBLs blazars become more prevalent, particularly beyond $z = 1$.
The decline in HBL detections beyond $z = 1$ in the *Fermi*-LAT sample aligns with the cut-off seen in IACTs TeV-detected sources: the cosmological effects impose a maximum horizon for blazars detectable in the TeV band with current technology.
The *Fermi*-LAT sample shows a different detection limit for the different SED type. HBLs are detected up to $z = 2$, whereas LBLs or FSRQs continue to be observed at higher redshifts. This trend can be explained by the fact that HBLs are intrinsically less luminous. As a result, the decline in observed flux due to distance makes it increasingly difficult to detect HBLs beyond a certain redshift, as they become too faint for detection. On the other hand, LBLs and FSRQs, due to their higher intrinsic luminosity, would exhibit a greater flux at the same redshift, making them easier to observe. Moreover, according to the interpretation of the blazar sequence as an evolutionary track, HBLs are considered the final stage in the evolution of blazars, transitioning from LBLs and FSRQs. Consequently, in earlier cosmic epochs, fewer HBLs would be expected, since the blazars would still be in an earlier evolutionary stage, exhibiting the characteristics of FSRQs and LBLs.

Moreover, it is important to note that although IACTs are primarily sensitive to detecting HBLs, whose IC peak lies around 100 GeV, it is not surprising to observe LBLs and FSRQs at higher redshifts. Even though these blazars have an IC peak in the GeV domain, the high-energy tail of their emission can extend into the TeV range, placing them within the detectability domain of IACTs. This occurs

especially when these sources exhibit flares, when their luminosity significantly increases. As a result, the more distant sources detected by IACTs, often during flaring states, are typically LBLs and FSRQs, which generally experience less absorption from the EBL, and thus can be observed at higher redshift. Referring to Figure 2.7, it can be observed that for $z = 0.5$, which marks the redshift where HBLs detections by IACTs stop, the attenuation factor $\tau \approx 3$ for 1 TeV photons. In contrast, for 0.5 TeV (500 GeV) photons, at $z = 0.5$, $\tau \approx 1$, and it only drops to $\tau \approx 3$ at $z \approx 1$, which represents the maximum observational horizon of IACTs.

The next section presents the synchrotron peak flux distribution, highlighting the differences in flux sensitivity between IACTs and *Fermi*-LAT, and how these impact the detected blazar populations.

4.3 Synchrotron Peak Flux Distribution

In Figure 4.7 are reported the synchrotron peak flux distribution for the two samples, color coded by SED type. The total height of each column represents the total number of blazars at that redshift. The colored segments within each column indicate the number of blazars belonging to each specific class.

IACTs: the IACTs histogram, on the left in figure 4.7, shows a range of fluxes mostly concentrated between $\log \nu F_\nu = -12$ and $\log \nu F_\nu = -10$, with a peak around $\log \nu F_\nu = -11$. The majority of the sources are concentrated in this region, with very few blazars showing fluxes below $\log \nu F_\nu = -12$. This indicates that IACTs primarily detect nearby blazars, as seen in the previous section 4.2, which consequently have higher observed fluxes.

***Fermi*-LAT**: the *Fermi*-LAT histogram, on the right in Figure 4.7, presents a broader range of fluxes, spanning from $\log \nu F_\nu = -14$ to $\log \nu F_\nu = -10$. Most blazars fall within the flux range $\log \nu F_\nu = -13$ to $\log \nu F_\nu = -11$, with a clear peak around $\log \nu F_\nu = -12$. *Fermi*-LAT captures a significant number of blazars with fluxes lower than $\log \nu F_\nu = -12$. This indicates its capability to detect more distant blazars, which therefore have weaker fluxes.

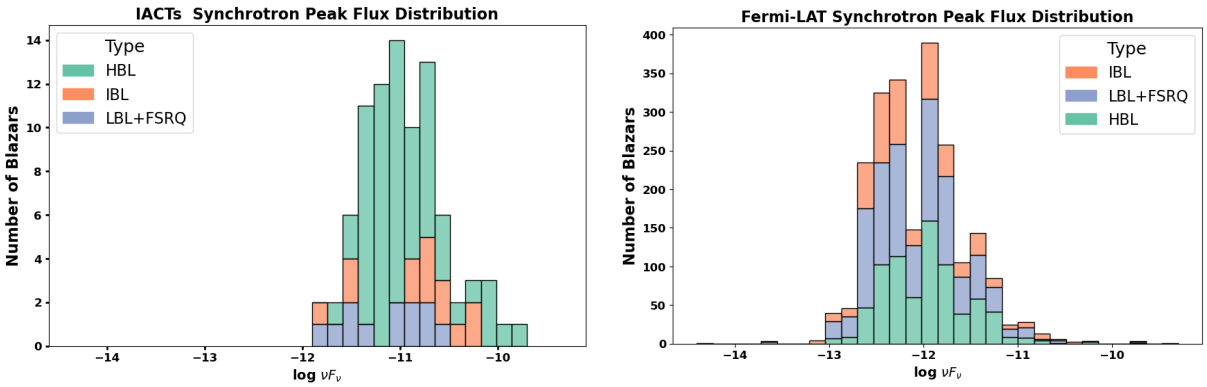

Figure 4.7: Left: IACTs synchrotron peak flux distribution color-coded by blazar type. Right: *Fermi*-LAT synchrotron peak flux distribution color-coded by blazar type.

The comparison between the two distributions suggests that IACTs detect the high-value tail of the $\log \nu F_\nu$ distribution observed by *Fermi*-LAT. In fact, the IACTs distribution is narrower and peaks

around $\log \nu F_\nu = -11$, which corresponds to the region where the tail of the *Fermi*-LAT distribution extends. *Fermi*-LAT exhibits a broader flux distribution, reflecting its ability to observe blazars over a wide range of distances. This indicates that IACTs predominantly observe nearby blazars with higher observed fluxes, due to their closer proximity.
Furthermore, the difference in time response between the instruments (see Fig. 4.5), as discussed in the previous section, allows IACTs to capture flaring events from blazars, which correspond to very high flux states. On the other hand, *Fermi*-LAT is less effective at detecting transient phenomena such as flares due to its longer time response, and its blazar population consists of blazars not in a flaring state, thus never measuring fluxes as high as those observed by IACTs. This is consistent with the characteristics of the two instruments: IACTs target very high-energy gamma rays and efficiently detect flares, while *Fermi*-LAT is optimized for lower-energy gamma rays and miss flare events. Additionally, considering that IACTs perform a pointed observation strategy, targeting the most promising sources, an additional observational selection bias must be taken into account. This method results in a sample of blazars with higher observed fluxes, as the sources with higher fluxes are preferentially chosen for observation. Unlike IACTs, *Fermi*-LAT conducts a full-sky survey, which leads to a broader flux distribution.

4.4 CTAO

In this section, the TeV and GeV blazar population are compared in relation to future observation by CTAO. Currently, 86 blazars are detected in the TeV range, while more than 3000 blazars have been observed in the GeV range. CTAO is expected to increase the number of TeV-detected blazars, and an estimate of this improvement is provided here.

A plot was created with the synchrotron peak frequency $\nu_{\rm p}$ and synchrotron peak flux νF_ν, considering only blazars with $\nu_{\rm p} > 10^{13.5}$ Hz, thereby excluding LBLs and FSRQs. This choice comes from the fact that the synchrotron peak flux is an indicative parameter for the inverse compton (IC) peak flux only when the relative heights of the two peak do not vary significantly. According to the blazar sequence, the ratio between the synchrotron and the IC peaks is ~ 1:1 only for HBLs (see 2.3). As the transition from HBLs to LBLs and FSRQs occurs, the IC peak becomes higher. Additionally, regardless of CTAO improvements, LBLs and FSRQs primarily have their high-energy peak in the GeV range, with an emission mostly falling out of the IACTs energy range.

IACTs are not sensitive to synchrotron frequencies; however, as discussed earlier, in cases where there is no significant Compton dominance, the overall energy distributions of the synchrotron and IC peaks are similar (although the IC peak is normally narrower in frequencies than the synchrotron peak). Using this consideration, one can cast the IACTs sensitivity to the IC peak into the synchrotron peak by a translation of the sensitivity curve to synchrotron peak energies. Obviously, this is not a physically driven procedure, which can be done only when a physical model is applied to all the multiwavelength data as well as considering the redshift and the EBL absorption. However, as demonstrated later, this approach allows for a reasonably accurate estimation of the sensitive regions of current IACTs and provides predictions for those of CTAO. The expected detection limit of CTAO is obtained by improving the IACTs sensitivity curve by a factor of 0.6. This estimation is based on sen-

sitivity data comparing CTAO North and South with the other IACTs MAGIC, H.E.S.S, and VERITAS, showed in figure 4.8. The difference in sensitivity was evaluated at an energy of 10^{-1} TeV (100 GeV), where CTAO's sensitivity is approximately 0.6 orders of magnitude higher than that of MAGIC, which was chosen as representative of other IACTs, given that more than 50% of TeV blazars have been observed by MAGIC. The choice of 100 GeV for the threshold energy sensitivity was made because it is roughly the boundary between the sensitivity ranges of *Fermi*-LAT and IACTs, and since most of the sources in this study were not observed at 1 TeV, 100 GeV is the most reasonable choice. Additionally, this is a conservative estimate, as CTAO improvement is less pronounced at this energy compared to higher ones.

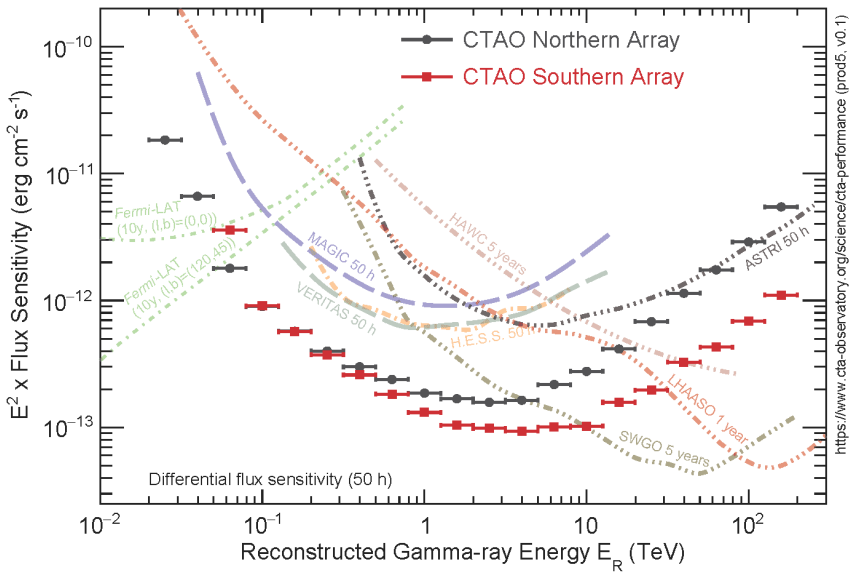

Figure 4.8: CTAO North and South vs. other gamma instrument sensitivity. [4]

First, to test the consistency of the detection limit traced for the IACTs, a plot 4.9 was produced that displays $\log \nu_p$ and $\log \nu F_\nu$ values for HBLs and IBLs blazars with $z < 1$, observed by MAGIC, VERITAS, and H.E.S.S in red, and by *Fermi*-LAT in blue. The detection limit of IACTs is shown in green. The points are aligned vertically and horizontally in a grid-like pattern because Firmamento, from which the parameters were obtained, provides values that vary only by 0.1. The darker points indicate overlapping sources that share the same values, which makes the points appear denser and darker blue or red. Some red points, representing TeV blazars, lie below the IACTs detection limit because these blazars were observed during flare states, where their flux was temporarily much higher than in the quiescent state. The parameters used, extracted by Firmamento, represent the averaged synchrotron peak values from all available data, including periods when the blazars were not flaring, so the values plotted do not reflect the elevated flux levels that allowed IACTs to detect these blazars.

The redshift limit $z < 1$ was considered because it corresponds to the observational limit of current IACTs. These limits, as already discussed in section 4.2, are due to the EBL, which hinders the detection of VHE photons from distant sources. Considering that IACTs typically detect non-flaring blazars at $z < 0.3$, the expected number of blazars above the detection limit in the plot would cor-

[4] From https://www.ctao.org

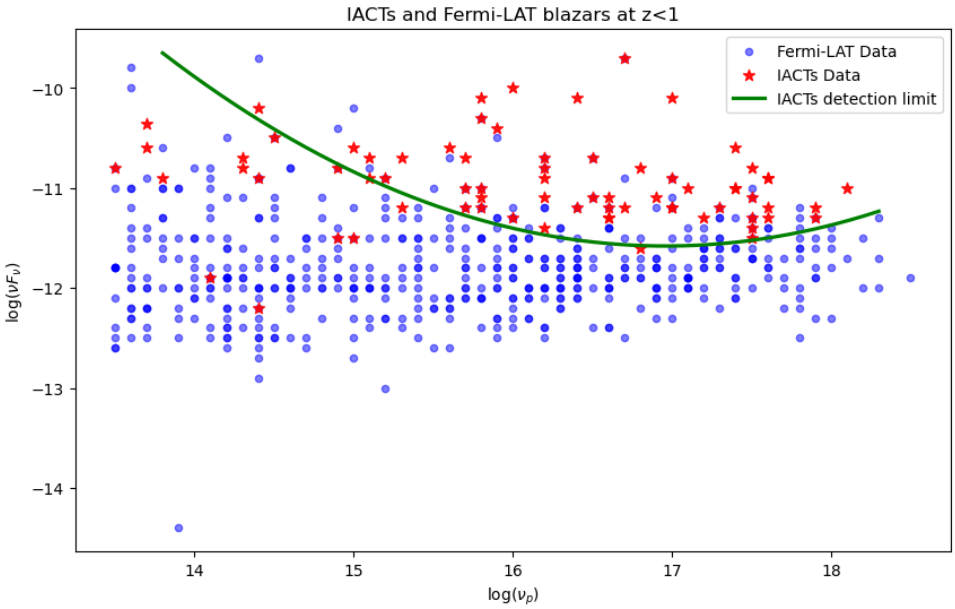

Figure 4.9: Scatter plot $\log \nu_{\rm p}$ vs. $\log \nu F_\nu$ for IACT's and *Fermi*-LAT IBLs and HBLs blazars $z < 1$.

respond to the total number of TeV sources detected within this redshift, which is 63 in total. As mentioned earlier, the synchrotron peak flux extracted by Firmamento is based on the analysis of all available data and, therefore, is not indicative of the flux at which the sources were detected by the IACTs. From the distribution of sources in the plot, it can be observed that there are **57** TeV-detected blazars above the green line. Thus, the green curve is consistent with the detection limit of current IACTs.

Now, estimates can be made based on these results in anticipation of CTAO. It is expected that CTAO will push beyond the current IACTs limit of $z = 1$. However, despite the improved sensitivity of the instruments, TeV observations are also constrained by the effects of EBL. Consequently, to make estimates on future CTAO observations, the previous plot was modified by selecting only sources with $z < 1.5$, adopting an upper redshift limit for a more cautious approach when making predictions. This choice stems from the detectability limits of HBLs, which emit in the TeV range, by *Fermi*-LAT, set at $z = 1.5$ (see 4.2).

In the new plot 4.10 the detection limit for CTAO, shown in purple, has been added by improving the IACTs sensitivity curve by a factor of 0.6. From the plot, it can be observed that there are **5** TeV blazars located between the green and purple lines. These blazars, which have only been detected in a flaring state by current IACTs, could potentially be detected in their quiescent state by CTAO. Furthermore, there are **254** GeV-detected sources situated above the purple line. These blazars are all potential TeV sources that could be detected by CTAO, currently beyond the limit of existing IACTs.

This potential increase in the number of TeV-detected blazars brought by CTAO will expand the range of sources available for studying the properties and emission processes in the TeV domain occurring in blazars. This broader sample will provide a more comprehensive understanding of the mechanisms driving high-energy emissions, offering deeper insights into the physical conditions within the extreme environments of the blazar jet. In addition, strengthening the connection between GeV and TeV observations will offer a more complete view of the gamma-ray spectrum of blazars. This will improve the estimation of their total energy output, as the emission processes at different energy scales

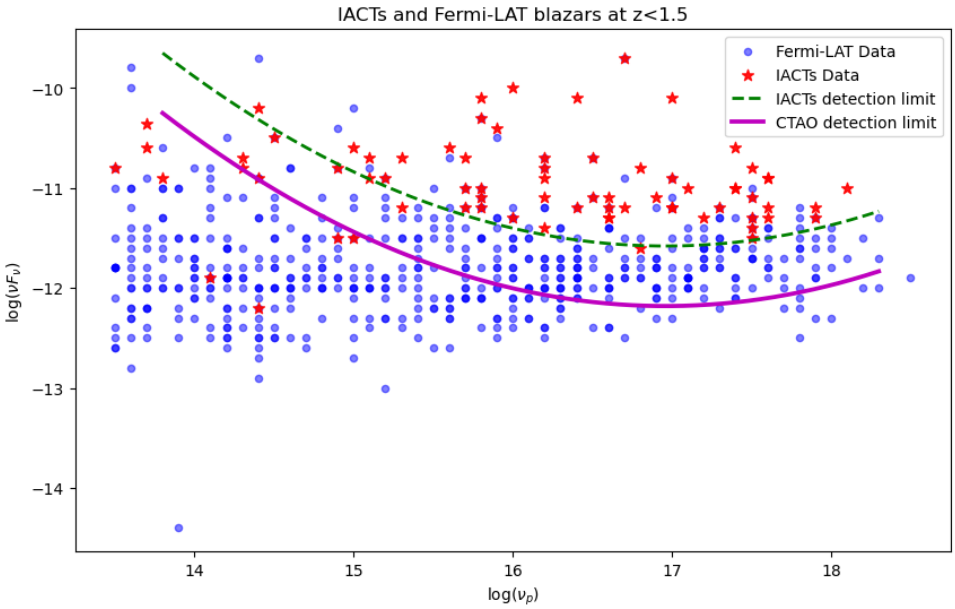

Figure 4.10: Scatter plot $\log \nu_{\mathrm{p}}$ vs. $\log \nu F_\nu$ for IACT's and *Fermi*-LAT IBLs and HBLs blazars at $z < 1.5$.

are closely interconnected. Moreover, having complete high-energy emission data provides the opportunity to better test emission models by constraining the involved parameters, particularly in the case of the Synchrotron Self-Compton (SSC) model, which does not require external parameters outside the jet to be considered.

Chapter 5

Conclusion

The analysis conducted in this thesis on the populations of blazars observed in the GeV and TeV bands highlights significant differences between the two, driven by both instrumental sensitivities and the intrinsic properties of the blazars.
The TeV blazar population is characterized by nearby blazars, all detected up to $z = 1$, with a synchrotron peak distribution concentrated at high frequencies, dominated by HBLs. This is expected, as these blazars emit strongly in the TeV range. The flux distribution for TeV blazars is narrower and centered around higher flux values, reflecting both the fact that IACTs primarily observe nearby blazars, which naturally have higher fluxes, and the selection bias due to IACTs targeting the most promising sources, often in a flaring state.
The GeV blazar population, observed by *Fermi*-LAT, has a broader redshift distribution extending up to $z = 3.5$. The synchrotron peak distribution is also wide, with a predominance of IBLs, LBLs, and FSRQs. The flux distribution in this population is broader as well, centered around lower values compared to the IACTs, reflecting the greater distances at which *Fermi*-LAT can observe, thus also detecting lower fluxes from more distant sources.
The redshift analysis of the two populations reveals constraints for the SED types of blazars. In both populations, HBLs are detected at lower redshifts, becoming increasingly less numerous as redshift increases. Specifically, it was observed that HBLs are predominantly detected at $z < 0.3$ in the TeV population and at $z < 1.5$ in the GeV population. As the redshift increases, IBLs and LBLs become more numerous. This distribution reflects the effects of EBL absorption, which significantly impacts VHE photons, limiting the detectability of HBLs in the TeV range by IACTs. Moreover, the lower intrinsic luminosity of HBLs makes them more difficult to detect at greater distances by *Fermi*-LAT. Thanks to their higher luminosity, LBLs and FSRQs can be detected at higher redshifts.

Using the results of the analysis, it was possible to extrapolate the number of GeV-detected blazars that could be observable in the TeV band by CTAO. By considering the synchrotron peak flux and frequency of both samples, and excluding LBLs and FSRQs whose emissions are predominantly in the GeV range, detection limits for both current IACTs and the expected performance of CTAO were derived. It was estimated that CTAO will be able to detect in TeV range 254 GeV-detected blazars. To improve the reliability of this estimate, future work could involve modeling the SEDs of these TeV candidate blazars to determine how closely their emissions fall within the sensitivity threshold of CTAO. Utilizing tools like the Markarian Multiwavelength Data Center would enable the creation of

detailed SED models based on multi-wavelength data. This approach would help to better select the most promising targets for future observations, optimizing the observational strategy of CTAO to increase the likelihood of successful detection.

Appendix A

Appendix

Name	RA	DEC	Redshift
PKS 1424+240	14 27 00	+23 47 40	0.16 †
H 1722+119	17 25 04.3	+11 52 15	0.018 †
Markarian 421	11 04 19	+38 11 41	0.031
Markarian 501	16 53 52.2	+39 45 37	0.034
1ES 2344+514	23 47 04	+51 42 49	0.044
Markarian 180	11 36 26.4	+70 09 27	0.045
1ES 1959+650	19 59 59.8	+65 08 55	0.047
AP Librae	15 17 41.8	-24 22 19	0.049
TXS 0210+515	02 14 17.9	+51 44 52	0.049
1ES 2037+521	20 39 23.5	+52 19 50	0.053
1ES 1727+502	17 28 18.6	+50 13 10	0.055
PGC 2402248	07 33 26.7	+51 53 53.9	0.065
PKS 0548-322	05 50 38.4	-32 16 12.9	0.069
BL Lacertae	22 02 43.3	+42 16 40	0.069
PKS 2005-489	20 09 27.0	-48 49 52	0.071
RGB J0152+017	01 52 33.5	+01 46 40.3	0.08
1ES 1741+196	17 44 01.2	+19 32 47	0.084
SHBL J001355.9-185406	00 13 52.0	-18 53 29	0.095
RGB J2056+496	20 56 42.7	+49 40 07	0.1 †
W Comae	12 21 31.7	+28 13 59	0.102
RGB J2042+244	20 42 06	+23 26 52.3	0.104
MG2 J204208+2426	20 42 6.05	+24 26 52.34	0.104
1ES 1312-423	13 14 58.5	-42 35 49	0.105
MS 13121-4221	13 15 3.39	-42 36 49.76	0.106
TXS 0518+211	05 21 45.97	+21 12 51.45	0.108 †
PKS 2155-304	21 58 52.7	-30 13 18	0.116
B2 1811+31	18 13 35.2027	+31 44 17.620	0.117
B3 2247+381	22 50 06.6	+38 25 58	0.119
1RXS J195815.6-301119	19 58 14.9	-30 11.8	0.119329

Name	RA	DEC	Redshift
RGB J0710+591	07 10 26.4	+59 09 00	0.125
TXS 1515-273	15 18 03.610	-27 31 34.40	0.1285
H 1426+428	14 28 32.6	+42 40 21	0.129
1ES 1215+303	12 17 48.5	+30 06 06	0.131
RX J1136.5+6737	11 36 30.1	+67 37 04	0.1342
1ES 0806+524	08 09 59	+52 19 00	0.138
PKS 1440-389	14 44 00.2	-39 08 21	0.1385
1ES 0229+200	02 32 48.61	+20 17 17.49	0.139
1RXS J101015.9-311909	10 10 15.03	-31 18 18.4	0.142639
1ES 1440+122	14 43 15	+12 00 11	0.163
H 2356-309	23 59 09.42	-30 37 22.7	0.165
1RXS J081201.8+023735	08 12 15.20	+02 37 33.10	0.1721
1ES 2322-409	23 24 48.0	-40 39 36.0	0.1736
MAGIC J2001+435	20 01 15.6	+43 52 44.4	0.173
RX J0648.7+1516	06 48 45.6	+15 16 12	0.179
PG 1218+304	12 21 21.94	+30 10 37.16	0.184
1ES 1101-232	11 03 36.5	-23 29 45	0.186
1ES 0347-121	03 49 23.0	-11 58 38	0.188
PKS 0736+017	07 39 17.0	+01 36 12	0.189
RBS 0413	03 19 47	+18 45 42	0.19
RBS 0723	08 47 12.9	+11 33 50	0.198
MRC 0910-208	09 13 00.22	-21 03 21.1	0.198 †
1ES 0647+250	06 50 46.5	+25 03 00	0.203 †
HESS J1943+213	19 43 55	+21 18 08	0.21
1ES 1011+496	10 15 04.1	+49 26 01	0.212
MS 1221.8+2452	12 24 24.2	+24 36 24	0.218
S5 0716+714	07 21 53.4	+71 20 36	0.2315
1RXS J023832.6	02 38 32.5	-31 16 58	0.232
RBS 1366	14 17 56.667	+25 43 26.22	0.236
PKS 1413+135	14 15 58.8	+13 20 23.7	0.247 †
S2 0109+22	01 12 05.8	+22 44 39	0.265
PKS 0301-243	03 03 23.49	-24 07 35.86	0.2657
1ES 0414+009	04 16 52.96	+01 05 20.4	0.287
OJ 287	08 54 49.1	+20 05 58.89	0.306
OT 081	17 51 32.82	+09 39 00.73	0.322
S3 1227+25	12 30 14.1	+25 18 07	0.325
TXS 0506+056	05 09 25	+05 42 09	0.336
3C 66A	02 22 39.61	+43 02 07.80	0.34
1ES 0502+675	05 07 56.2	+67 37 24	0.34
PKS 0447-439	04 49 28.2	-43 50 12	0.343
PKS 1510-089	15 12 52.2	-09 06 21.6	0.36
1ES 1028+511	10 31 18.5184	+50 53 35.818	0.361

Name	RA	DEC	Redshift
S4 0954+65	09 58 47.00	+65 33 55.00	0.369
RGB J2243+203	22 43 52	+20 19 12	0.395
PG 1553+113	15 55 44.7	+11 11 41	0.43
4C +21.35	12 24 54.4	+21 22 46	0.432
1ES 0033+595	00 35 16.8	+59 47 24.0	0.467
GB6 J1058+2817	10 58 29.8949	+28 17 46.212	0.479 †
KUV 00311-1938	00 33 36	-19 21 00	0.5
3C 279	12 56 11.1	-05 47 22	0.536
B2 1420+32	14 22 30.38	+32 23 10.44	0.682
PKS 0903-57	09 04 53.1790	-57 35 05.783	0.695
TON 0599	11 59 31.8	+29 14 44	0.7247
RGB J0136+391	01 36 32.5	+39 06 00	0.75 †
PKS 1441+25	14 43 56.9	+25 01 44	0.939
S3 0218+35	02 21 05.5	+35 56 14	0.95
PKS 0346-27	03 48 38	-27 49 14	0.991

Table A.2: TeV blazar detected by MAGIC, H.E.S.S. and VERITAS. The redshifts marked with † are retrieved from NED, as they are not available in the TeVCat and STeVCat catalogs.

Bibliography

Abe, H et al. (Mar. 2024). "The variability patterns of the TeV blazar PG 1553 + 113 from a decade of MAGIC and multiband observations". In: *Monthly Notices of the Royal Astronomical Society* 529.4, pp. 3894–3911. ISSN: 1365-2966. DOI: 10.1093/mnras/stae649. URL: http://dx.doi.org/10.1093/mnras/stae649.

Abe, S. et al. (2023). *First characterization of the emission behavior of Mrk421 from radio to VHE gamma rays with simultaneous X-ray polarization measurements*. arXiv: 2312.10732 [astro-ph.HE]. URL: https://arxiv.org/abs/2312.10732.

Ackermann, M. et al. (Nov. 2012). "The Imprint of the Extragalactic Background Light in the Gamma-Ray Spectra of Blazars". In: *Science* 338.6111, pp. 1190–1192. ISSN: 1095-9203. DOI: 10.1126/science.1227160. URL: http://dx.doi.org/10.1126/science.1227160.

Atwood, W. B. et al. (May 2009). "THE LARGE AREA TELESCOPE ON THEFERMI GAMMA-RAY SPACE TELESCOPEMISSION". In: *The Astrophysical Journal* 697.2, pp. 1071–1102. ISSN: 1538-4357. DOI: 10.1088/0004-637x/697/2/1071. URL: http://dx.doi.org/10.1088/0004-637X/697/2/1071.

Ballet, J. et al. (2024). *Fermi Large Area Telescope Fourth Source Catalog Data Release 4 (4FGL-DR4)*. arXiv: 2307.12546 [astro-ph.HE]. URL: https://arxiv.org/abs/2307.12546.

Bégué, D. et al. (Mar. 2024). "Modeling Blazar Broadband Emission with a Convolutional Neural Network. I. Synchrotron Self-Compton Model". In: 963.1, 71, p. 71. DOI: 10.3847/1538-4357/ad19cf. arXiv: 2311.02979 [astro-ph.HE].

Bonnarel, F. et al. (Apr. 2000). "The ALADIN interactive sky atlas. A reference tool for identification of astronomical sources". In: 143, pp. 33–40. DOI: 10.1051/aas:2000331.

Chang, Y.-L., C.H. Brandt, and P. Giommi (Jan. 2020). "The Open Universe VOU-Blazars tool". In: *Astronomy and Computing* 30, p. 100350. ISSN: 2213-1337. DOI: 10.1016/j.ascom.2019.100350. URL: http://dx.doi.org/10.1016/j.ascom.2019.100350.

Cooray, Asantha (2016). *Extragalactic Background Light: Measurements and Applications*. arXiv: 1602.03512 [astro-ph.CO]. URL: https://arxiv.org/abs/1602.03512.

De Angelis, A., O. Mansutti, and M. Persic (July 2008). "Very-high-energy gamma astrophysics". In: *La Rivista del Nuovo Cimento* 31.4, pp. 187–245. ISSN: 0393697X, 0393697X. DOI: 10.1393/ncr/i2008-10032-2. URL: https://doi.org/10.1393/ncr/i2008-10032-2.

Donath, Axel et al. (Oct. 2023). "Gammapy: A Python package for gamma-ray astronomy". In: *Astronomy amp; Astrophysics* 678, A157. ISSN: 1432-0746. DOI: 10.1051/0004-6361/202346488. URL: http://dx.doi.org/10.1051/0004-6361/202346488.

Doro, Michele et al. (2019). *Toward a Public MAGIC Gamma-Ray Telescope Legacy Data Portal*. arXiv: 1909.01172 [astro-ph.IM]. URL: https://arxiv.org/abs/1909.01172.

Fossati, G. et al. (Sept. 1998). “A unifying view of the spectral energy distributions of blazars”. In: *Monthly Notices of the Royal Astronomical Society* 299.2, pp. 433–448. ISSN: 1365-2966. DOI: 10.1046/j.1365-8711.1998.01828.x. URL: http://dx.doi.org/10.1046/j.1365-8711.1998.01828.x.

Franceschini, A., G. Rodighiero, and M. Vaccari (June 2008). “Extragalactic optical-infrared background radiation, its time evolution and the cosmic photon-photon opacity”. In: *Astronomy & Astrophysics* 487.3, pp. 837–852. ISSN: 1432-0746. DOI: 10.1051/0004-6361:200809691. URL: http://dx.doi.org/10.1051/0004-6361:200809691.

Ghisellini, G., C. Righi, et al. (Apr. 2017). “The Fermi blazar sequence”. In: *Monthly Notices of the Royal Astronomical Society* 469.1, pp. 255–266. ISSN: 1365-2966. DOI: 10.1093/mnras/stx806. URL: http://dx.doi.org/10.1093/mnras/stx806.

Ghisellini, G., F. Tavecchio, et al. (May 2011). “The transition between BL Lac objects and flat spectrum radio quasars: FSRQs and BL Lacs”. In: *Monthly Notices of the Royal Astronomical Society* 414.3, pp. 2674–2689. ISSN: 0035-8711. DOI: 10.1111/j.1365-2966.2011.18578.x. URL: http://dx.doi.org/10.1111/j.1365-2966.2011.18578.x.

Ghisellini, Gabriele (2013). *Radiative Processes in High Energy Astrophysics*. Springer International Publishing. ISBN: 9783319006123. DOI: 10.1007/978-3-319-00612-3. URL: http://dx.doi.org/10.1007/978-3-319-00612-3.

Glauch, Theo, Tobias Kerscher, and Paolo Giommi (2022). *BlaST – A Machine-Learning Estimator for the Synchrotron Peak of Blazars*. arXiv: 2207.03813 [astro-ph.HE]. URL: https://arxiv.org/abs/2207.03813.

Gréaux, Lucas et al. (2023). *STeVECat, the Spectral TeV Extragalactic Catalog*. arXiv: 2304.00835 [astro-ph.HE]. URL: https://arxiv.org/abs/2304.00835.

Hinrichs, Claire E., Atreya Acharyya, and Alberto C. Sadun (2023). “Multi-wavelength Observations of a Long-duration Flare from BL Lacertae”. In: *Proceedings of 38th International Cosmic Ray Conference — PoS(ICRC2023)*. Vol. 444, p. 747. DOI: 10.22323/1.444.0747.

Longair, Malcolm S. (2011). *High Energy Astrophysics*. 3rd ed. Cambridge University Press.

Prandini, Elisa, Konstantinos Dialektopoulos, and Jelena Strišković (Nov. 2022). “Gamma rays: propagation and detection”. In: *Proceedings of Corfu Summer Institute 2021 “School and Workshops on Elementary Particle Physics and Gravity” — PoS(CORFU2021)*. CORFU2021. Sissa Medialab. DOI: 10.22323/1.406.0319. URL: http://dx.doi.org/10.22323/1.406.0319.

Primack, Joel R. et al. (2011). “Extragalactic Background Light and Gamma-Ray Attenuation”. In: *AIP Conference Proceedings*. AIP, pp. 72–83. DOI: 10.1063/1.3635825. URL: http://dx.doi.org/10.1063/1.3635825.

Sahakyan, N. et al. (Aug. 2024). “Modeling Blazar Broadband Emission with Convolutional Neural Networks. II. External Compton Model”. In: 971.1, 70, p. 70. DOI: 10.3847/1538-4357/ad5351. arXiv: 2402.07495 [astro-ph.HE].

Sitarek, Julian et al. (2013). *Physics performance of the upgraded MAGIC telescopes obtained with Crab Nebula data*. arXiv: 1308.0141 [astro-ph.IM]. URL: https://arxiv.org/abs/1308.0141.

Sol, Hélène and Andreas Zech (Nov. 2022). “Blazars at Very High Energies: Emission Modelling”. In: *Galaxies* 10.6, p. 105. ISSN: 2075-4434. DOI: 10.3390/galaxies10060105. URL: http://dx.doi.org/10.3390/galaxies10060105.

Tripathi, Dhurba et al. (2024). *Firmamento: a multi-messenger astronomy tool for citizen and professional scientists*. arXiv: 2311.15102 [astro-ph.HE]. URL: https://arxiv.org/abs/2311.15102.

Urry, C. Megan and Paolo Padovani (Sept. 1995). "Unified Schemes for Radio-Loud Active Galactic Nuclei". In: *Publications of the Astronomical Society of the Pacific* 107, p. 803. ISSN: 1538-3873. DOI: 10.1086/133630. URL: http://dx.doi.org/10.1086/133630.